Mitja Trkov[1]
Department of Mechanical Engineering,
University of Utah,
Salt Lake City, UT 84112
e-mail: m.trkov@utah.edu

Kuo Chen[1]
Department of Mechanical and
Aerospace Engineering,
Rutgers University,
Piscataway, NJ 08854
e-mail: kc625@rutgers.edu

Jingang Yi[2]
Fellow ASME
Department of Mechanical and
Aerospace Engineering,
Rutgers University,
Piscataway, NJ 08854
e-mail: jgyi@rutgers.edu

Bipedal Model and Hybrid Zero Dynamics of Human Walking With Foot Slip

Foot slip is one of the major causes of falls in human locomotion. Analytical bipedal models provide an insight into the complex slip dynamics and reactive control strategies for slip-induced fall prevention. Most of the existing bipedal dynamics models are built on no foot slip assumption and cannot be used directly for such analysis. We relax the no-slip assumption and present a new bipedal model to capture and predict human walking locomotion under slip. We first validate the proposed slip walking dynamic model by tuning and optimizing the model parameters to match the experimental results. The results demonstrate that the model successfully predicts both the human walking and recovery gaits with slip. Then, we extend the hybrid zero dynamics (HZD) model and properties to capture human walking with slip. We present the closed-form of the HZD for human walking and discuss the transition between the nonslip and slip states through slip recovery control design. The analysis and design are illustrated through human walking experiments. The models and analysis can be further used to design and control wearable robotic assistive devices to prevent slip-and-fall. [DOI: 10.1115/1.4043360]

1 Introduction

Foot slip is one of the major causes for human falls and injuries. Slip-induced falls cause enormous economic and societal costs [1]. The direct costs for nonfatal fall-related injuries among U.S. elderly ($\geq$65 years) were \$19 billion in the year 2000 [1] and increased to over \$31 billion in the year 2015 [2]. Among the occupational population in the U.S., slips, trips, and falls represented 27% of all nonfatal occupational injuries in the year 2015 [3]. To develop effective fall prevention strategies and technologies, it is critical to understand human locomotion and balance recovery under slip. Modeling of human walking locomotion with slip is an effective approach to assist in the design and control of new wearable assistive devices. Slip-and-fall has been extensively studied in the past two decades, for example, Refs. [4,5] and references therein. Most of these studies focus on human subjects and clinical experiments and a few use human locomotion dynamics to analyze the slipping mechanism. Simulation-based dynamic models are used to study motion stability of slip and fall. In Ref. [5], a seven-link, nine-degrees-of-freedom (DOF) walking model in the sagittal plane with a 16-element foot model is used to simulate the human reaction control to a novel slip in gait. In Ref. [6], a simulation model is optimized with human experiments. Using this model, stability results are obtained and compared with the dynamic balance analyses by a simple invented pendulum model. The 2D musculoskeletal model in the sagittal plane is also discussed in Ref. [7] to determine the impact of the reduced required coefficient of friction (RCOF) on gait kinematics. Kinematic and muscle activity-based data-driven analysis (e.g., Lyapunov exponents) is used to capture the walking stability [8].

Robotic bipedal models [9,10] were recently presented for study of human walking gait [11,12], for design of prosthetic devices for lower-limbs [11] and control of robotic walkers. In Ref. [13], a bipedal model is proposed to study human gaits with fixed ankle joints. Both the single- and double-stance phases are included in the model and a hybrid zero dynamic (HZD) control is designed to track the human gait profile. Although the kinematic variables such as hip; knee; and head, arms, and trunk (HAT) joint angles match the human gaits, the predicted ground reaction forces (GRFs) have large discrepancies with experiments. In Ref. [12], only single-stance locomotion is considered in the model without the HAT. The models in Refs. [12] and [13] use the circular curved foot-floor contact that was developed in Ref. [14]. However, all of the above-mentioned bipedal models are built on the assumption that the foot-floor contact friction forces are large enough to prevent the foot from slipping, and thus, cannot be directly used to study slip-and-fall walking gaits. Bipedal walking is commonly described by a hybrid dynamics framework with continuous dynamics during the single- or double-stance periods with discrete mappings to capture the foot contact impacts. Using the HZD concept [15], a low-dimensional normal human walking model is presented in Ref. [13] and a state feedback control is designed to track the gait profile parameterized by the stance phase variable, rather than time [9]. The repetitive human walking gait is captured by the HZD when the gaits follow the desired profiles.

The goal of this study is to develop an analytic bipedal model and extend the HZD approach for human walking with slip. The model extends the bipedal framework in Refs. [9,11], and [12] by relaxing the foot no-slip assumption and using the circular rolling feet to capture the foot rolling characteristics. The proposed human walking model is built on a seven-link robotic bipedal dynamics model with actuated ankle joints. The model includes the dynamics of both the single- and double-stance motion. The model explicitly considers the foot slipping displacement, and therefore, can predict the human gait under slips. Moreover, we explicitly calculate and present the HZD that consists of dynamics of the gait progression variable and the slipping distance. The inclusion of the latter parameter is new compared to the existing HZD models. The HZD stability conditions and properties are also discussed under a set of slip recovery gaits that are obtained from human subject experiments. This paper extends the previous conference publications [16,17] by providing additional details in bipedal model derivation, model validation, and detailed HZD analyses of slip recovery stability examples and experiments.

The main impact of this work lies in the development of bipedal model and HZD slip analysis that provides an important insight into slip balance recovery analysis. This analytic analysis enables determination of the outcome of the balance recovery and distinguishing between successful versus unsuccessful slip balance

[1]M. Trkov and K. Chen equally contributed to this work.
[2]Corresponding author.

Contributed by the Design Engineering Division of ASME for publication in the Journal of Computational and Nonlinear Dynamics. Manuscript received August 8, 2018; final manuscript received March 27, 2019; published online September 12, 2019. Assoc. Editor: Elena G. Tolkacheva.

recovery, based on a current state/posture and angular momentum of the human model. The slip balance recovery analysis can be used in controller design of wearable robotic assistive devices for slip-and-fall prevention. Information of the required angular momentum for successful slip recovery based on the current states (i.e., joint angles, foot placement, and center of pressure (COP)) can be used to determine the required assistive torques provided by the device or repositioning of the foot placement to prevent falls.

The measurement of slipperiness and the devices to obtain the shoe-floor friction are discussed in Ref. [18]. Force plate is the most commonly used device to measure the GRF and used to calculate the foot contact COP. However, force plates cannot be used for monitoring daily activities outside the laboratory. In recent years, wearable insole pressure measurement devices were developed to obtain the GRF (e.g., Refs. [19] and [20]). In this work, we use an integrated sensor suite inside each shoe to measure the 3D GRF and torques. The details of these sensors are discussed in Ref. [21]. Combining with the wearable motion sensors (e.g., Ref. [22]), we obtain the limb poses and forces in indoor or outdoor environments.

The results in this paper complement the existing literature on human bipedal models and gait control. The main contributions of this work are threefold. First, this work extends the robotic bipedal models to study human walking under foot slip. The new model not only predicts the human gait with slip but also helps to understand the motion stability during slip. Second, besides relaxing the assumption of nonslip foot-floor contact, the new model brings innovative features and properties compared with the existing bipedal models. For example, compared with the bipedal models with a point, a flat or multicontact foot in Refs. [9] and [23–25], the new model includes an experimentally validated foot-floor contact circular shaped foot. Unlike the bipedal model in Ref. [12] that only deals with a single-stance human locomotion, the proposed model includes the human trunk (e.g., seven-link) and also the double-stance phase, which is crucial for slips and fall motion. Compared with the work in Refs. [11] and [13], the proposed model includes the active ankle joints and also generates the matched GRF with the experiments. Third, we present the new HZD model and its application to human walking under foot slip. The HZD can be used to analytically investigate the slip balance stability and recovery strategies that are otherwise not possible through clinical studies.

The rest of the paper is organized as follows. We first present the bipedal dynamic model for normal walking gait without slip in Sec. 2. In Sec. 3, we present the bipedal model for walking with slips. Section 4 presents hybrid zero dynamics for no-slip walking and slip gait. The experiments and results are presented in Sec. 5. The discussion of the results is presented in Sec. 6. We conclude the paper and discuss the future work in Sec. 7.

2 Bipedal Walking Model Without Slips

2.1 System Configuration. Figure 1(*a*) illustrates the setup of the coordinates for bipedal modeling of human walking. The human motion is considered only in the sagittal plane. The human body is considered as a seven-link rigid body. The HAT is considered as one link that is connected to the left and the rightthigh. The model has two active hip joints, two active knee joints, and two active ankle joints. Similar to those in Ref. [12], we use relative angles q_i, $i = 2, \ldots, 7$, to define the configuration of the system and the absolute angle q_1 denotes the leading stance leg orientation with respect to the vertical position.

We define the joint angle vector $\boldsymbol{q}_a = [q_1 \cdots q_7]^{\mathrm{T}}$. The foot-floor contact is considered as a circular disk with radius R rolling on the solid ground; see Fig. 1(*b*). To capture the slip motion of the foot, we denote the position of the rotating center O_r of the foot as $[x_o \;\; y_o]^{\mathrm{T}}$ and a slipping vector $\boldsymbol{q}_s = [x_s, y_s]^{\mathrm{T}} = [x_o + R(\phi - \phi_0), y_o - R]^{\mathrm{T}}$, where ϕ is the absolute rolling angle of the stance foot with respect to the vertical direction and ϕ_0 is the initial value of ϕ. $\dot{\boldsymbol{q}}_s = [\dot{x}_o + R\dot{\phi}, \dot{y}_o]^{\mathrm{T}}$ is the slipping velocity. When the stance foot is purely rolling on the ground, $\dot{\boldsymbol{q}}_s = \boldsymbol{0}$. We use $\boldsymbol{q}_s$ and $\boldsymbol{q}_a$ (i.e., foot rotating angle) to calculate the stance foot-floor contact point C. To completely determine the walking gait with slip, we define the generalized coordinate $\boldsymbol{q}_e = [\boldsymbol{q}_a^{\mathrm{T}} \;\; \boldsymbol{q}_s^{\mathrm{T}}]^{\mathrm{T}}$.

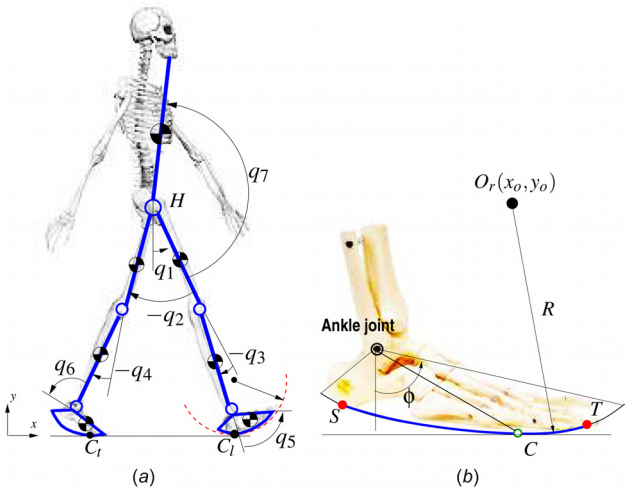

Fig. 1 (*a*) Schematic of the seven-link human walking model with curved foot contact and (*b*) schematic of the foot-contact model

A human walking cycle consists of a series of repeated sequential movements and events [9], namely a single-stance, a double-stance, and the foot impact phases. During the single-stance phase, the stance foot rolls on the ground, while the swing foot moves in the air from positions behind to front of the stance foot. Once the swing foot impacts on the ground (i.e., heel-touch), the joint velocity suddenly changes and the joint configuration is relabeled due to the switching role of the stance and swing legs. The double-stance phase refers to the stage when both legs roll on the ground. Finally, the trailing stance foot leaves the ground (i.e., toe-off) and the pose returns to the single-stance phase. Hybrid models shown in Fig. 2 are used to capture the above-mentioned discrete-continuous dynamics.

2.2 Single- and Double-Stance Models and Gait Controller. The nonslip single-stance dynamics are described as [9]

$$\Sigma_s: \; \boldsymbol{D}_s(\boldsymbol{q}_a)\ddot{\boldsymbol{q}}_a + \boldsymbol{C}_s(\boldsymbol{q}_a, \dot{\boldsymbol{q}}_a)\dot{\boldsymbol{q}}_a + \boldsymbol{G}_s(\boldsymbol{q}_a) = \boldsymbol{B}_s\boldsymbol{u} \tag{1}$$

where $\boldsymbol{D}_s(\boldsymbol{q}_a)$, $\boldsymbol{C}_s(\boldsymbol{q}_a, \dot{\boldsymbol{q}}_a)$, $\boldsymbol{G}_s(\boldsymbol{q}_a)$, and $\boldsymbol{B}_s$ are the inertia, Coriolis, gravity, and input mapping matrices, respectively. There are six joint torque inputs $\boldsymbol{u} \in \mathbb{R}^6$ and the system is underactuated since absolute joint angle q_1 is not controlled by any joint torque.

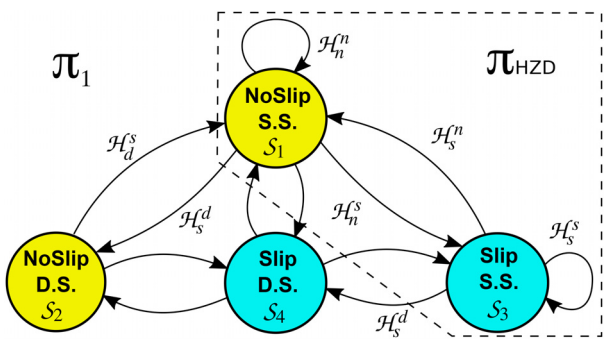

Fig. 2 Finite state diagram of human walking gait with slips

Therefore, we have $\boldsymbol{B}_s = [\boldsymbol{0}_{n-1}\ \boldsymbol{I}_{n-1}]^{\mathrm{T}}$, where $\boldsymbol{0}_n = [0 \cdots 0]^{\mathrm{T}} \in \mathbb{R}^n$ is a zero column vector and $\boldsymbol{I}_n$ is an n-dimensional identity matrix, where n represents a total number of joint angles ($n = 7$ in this paper). A feedback linearization approach is adopted to control the joint angles $\boldsymbol{q}_a$ to follow a desired trajectory that is specified by a progression variable $\theta = \boldsymbol{c}\boldsymbol{q}_a$, where $\boldsymbol{c}$ is a constant progression vector. During the single-stance phase, θ monotonically increases and the desired trajectory of actuated joint angles is expressed by θ. The feedback linearization controller enforces the virtual constraint specified by

$$\boldsymbol{y} = \boldsymbol{h}(\boldsymbol{q}_a) = \boldsymbol{H}_0\boldsymbol{q}_a - \boldsymbol{h}_d(\theta) = \boldsymbol{0} \tag{2}$$

where $\boldsymbol{H}_0$ is a constant matrix and $\boldsymbol{h}_d(\theta)$ is the desired trajectories of actuated joint angles described by the Bézier polynomials [9]. If $\boldsymbol{u}$ is properly chosen by feedback linearization to drive $\boldsymbol{y} = \dot{\boldsymbol{y}} = \boldsymbol{0}$, only the dynamics of θ is left as the zero dynamics [9].

To calculate the GRF for single-stance walking, we consider the dynamics of the individual link expressed as a function of joint angles, angular velocities, and accelerations. We sum these contributions to compute the instantaneous horizontal and vertical accelerations of the center of mass using forward kinematics. The external forces acting on the center of mass are the ground reaction forces and the gravitational force. Using Newtonian mechanics, it is straightforward to obtain the normal F_n and tangential force F_x at foot/ground contact points. This force calculation method is also generalized to the single-stance slip case discussed in Sec. 3.2.

During the double-stance phase, both the leading and trailing feet are in contact with the ground at contact points C_l and C_t, respectively; see Fig. 1(*a*). We consider a general modeling approach by defining slipping vectors $\boldsymbol{g}_l(\boldsymbol{q}_e) \in \mathbb{R}^2$ and $\boldsymbol{g}_t(\boldsymbol{q}_e) \in \mathbb{R}^2$ of contact points C_l and C_t, respectively. Note that both $\boldsymbol{g}_l(\boldsymbol{q}_e)$ and $\boldsymbol{g}_t(\boldsymbol{q}_e)$ are determined as functions of $\boldsymbol{q}_e$. Because of the foot-floor contact constraints, the equations of motion during the double-stance are expressed as

$$\Sigma_d : \boldsymbol{D}_e(\boldsymbol{q}_e)\ddot{\boldsymbol{q}}_e + \boldsymbol{C}_e(\boldsymbol{q}_e, \dot{\boldsymbol{q}}_e)\dot{\boldsymbol{q}}_e + \boldsymbol{G}_e(\boldsymbol{q}_e) = \boldsymbol{B}_e\boldsymbol{u} + \boldsymbol{E}_e^{\mathrm{T}}\boldsymbol{F}_e \tag{3}$$

where $\boldsymbol{D}_e(\boldsymbol{q}_e)$, $\boldsymbol{C}_e(\boldsymbol{q}_e, \dot{\boldsymbol{q}}_e)$, $\boldsymbol{G}_e(\boldsymbol{q}_e)$, and $\boldsymbol{B}_e$ are the inertia, Coriolis, gravity, and input mapping matrices, respectively. Matrix $\boldsymbol{E}_e = [(\partial \boldsymbol{g}_t(\boldsymbol{q}_e)/\partial \boldsymbol{q}_e)\ (\partial \boldsymbol{g}_l(\boldsymbol{q}_e)/\partial \boldsymbol{q}_e)]^{\mathrm{T}} \in \mathbb{R}^{4\times 9}$ describes the contact constraints and $\boldsymbol{F}_e = [F_{xt}\, F_{nt}\, F_{xl}\, F_{nl}]^{\mathrm{T}}$ is a vector of the collection of the tangential and normal forces at C_t and C_l, respectively. With nonslip conditions at C_l and C_t, we have four kinematic constraints $\boldsymbol{E}_e\dot{\boldsymbol{q}}_e = \boldsymbol{0}$ and the degrees-of-freedom given by Eq. (3) are $9 - 4 = 5$.

Since there are six active joints and five degrees-of-freedom, the bipedal system is overactuated. Using a similar derivation as in Ref. [13], the constrained dynamics is reformulated as

$$\boldsymbol{D}_{di}\ddot{\boldsymbol{q}}_{di} + \boldsymbol{C}_{di}\dot{\boldsymbol{q}}_{di} + \boldsymbol{G}_{di} = \boldsymbol{M}_{di}\boldsymbol{u} \tag{4}$$

where subscript "di" denotes double-stance independent variable dynamics and $\boldsymbol{q}_{di} = [q_1\ q_2\ q_3\ q_5\ q_7]^{\mathrm{T}}$ and $\boldsymbol{M}_{di} \in \mathbb{R}^{5\times 6}$ map the six joint torques into the five-dimensional dynamics. To predict double-stance human gaits by Eq. (4), a Bézier polynomial is used to parameterize the desired trajectory of $\boldsymbol{q}_{di}^d$ [9]. The control input $\boldsymbol{u}$ is designed such that $\ddot{\boldsymbol{q}}_{di} = \boldsymbol{D}_{di}^{-1}(\boldsymbol{M}_{di}\boldsymbol{u} - \boldsymbol{C}_{di}\dot{\boldsymbol{q}}_{di} - \boldsymbol{G}_{di}) = \ddot{\boldsymbol{q}}_{di}^d - \boldsymbol{K}_p(\boldsymbol{q}_{di} - \boldsymbol{q}_{di}^d) - \boldsymbol{K}_d(\dot{\boldsymbol{q}}_{di} - \dot{\boldsymbol{q}}_{di}^d)$, where $\boldsymbol{K}_p$ and $\boldsymbol{K}_d$ are constant gain matrices. To solve $\boldsymbol{u}$ in the above equation, we need an additional constraint because of the overactuation configuration. In our implementation, we assume a simple linear constraint of the joint torques $\boldsymbol{\rho}^{\mathrm{T}}\boldsymbol{u} = 0$, and $\boldsymbol{\rho} \in \mathbb{R}^6$ is determined by the single-stance joint torque profiles. This constraint is based on the underlying physical principle assumption that humans minimize the effort for walking. The linear constraint $\boldsymbol{\rho}^{\mathrm{T}}\boldsymbol{u} = 0$ is equivalent to minimizing the effort $\boldsymbol{u}^{\mathrm{T}}(\boldsymbol{\rho}\boldsymbol{\rho}^{\mathrm{T}})\boldsymbol{u}$.

To calculate the ground reaction forces $\boldsymbol{F}_e$, we take time derivative of the kinematic constraint $\boldsymbol{E}_e\dot{\boldsymbol{q}}_e = \boldsymbol{0}$. Stacking with the dynamics in Eq. (3), we obtain (argument variables in the coefficient matrices are dropped for clarity)

$$\underbrace{\begin{bmatrix} \boldsymbol{D}_e & -\boldsymbol{E}_e^{\mathrm{T}} \\ \boldsymbol{E}_e & \boldsymbol{0} \end{bmatrix}}_{\boldsymbol{D}_{\mathrm{ext}}} \begin{bmatrix} \ddot{\boldsymbol{q}}_e \\ \boldsymbol{F}_e \end{bmatrix} = \begin{bmatrix} \boldsymbol{B}_e \\ \boldsymbol{0} \end{bmatrix}\boldsymbol{u} - \begin{bmatrix} \boldsymbol{C}_e \\ \dot{\boldsymbol{E}}_e \end{bmatrix}\dot{\boldsymbol{q}}_e - \begin{bmatrix} \boldsymbol{G}_e \\ \boldsymbol{0} \end{bmatrix} \tag{5}$$

Since matrix $\boldsymbol{D}_{\mathrm{ext}}$ is full rank, both $\ddot{\boldsymbol{q}}_e$ and forces $\boldsymbol{F}_e$ are obtained with the known $\boldsymbol{u}$ from the above controller design.

2.3 Impacting Model. The impact dynamics are obtained by integrating the double stance dynamics equation (3) over the instantaneous impact time with certain neglections [9]

$$\boldsymbol{D}_e(\boldsymbol{q}_e^-)\dot{\boldsymbol{q}}_e^+ - \boldsymbol{D}_e(\boldsymbol{q}_e^-)\dot{\boldsymbol{q}}_e^- = \boldsymbol{E}_{el}^{\mathrm{T}}(\boldsymbol{q}_e^-)\delta\boldsymbol{F}_{el} + \boldsymbol{M}$$

where superscripts "+" and "–" indicate the instants just after and before the impact event, respectively. The impulse due to the impact on the leading foot is $\delta\boldsymbol{F}_{el} = \int_{0^-}^{0^+} \boldsymbol{F}_{el}(t)dt$, where $\boldsymbol{F}_{el}$ contains both the normal and tangential ground reaction forces. The GRF applied on the trailing foot $\boldsymbol{F}_{et}$ is not an impact force. The integration of Coriolis term $\boldsymbol{C}_e$ and the gravitational term $\boldsymbol{G}_e$ are relatively small and therefore neglected. The integration of input torque $\boldsymbol{M} = \int_{0^-}^{0^+} \boldsymbol{B}_e\boldsymbol{u}(t)dt$ is a constant determined from the experimental data. After the impact, the swing leg sticks on the ground and thus

$$\boldsymbol{E}_{el}\dot{\boldsymbol{q}}_e^+ = \boldsymbol{0}$$

where $\boldsymbol{E}_{el}(\boldsymbol{q}_e) = (\partial \dot{\boldsymbol{g}}_l/\partial \dot{\boldsymbol{q}}_e)(\boldsymbol{q}_e)$ is the Jacobian matrix of impacting foot contact point velocity $\dot{\boldsymbol{g}}_l$ with respect to $\dot{\boldsymbol{q}}_e$.

We clearly express the impact mapping $\mathcal{H}_s^d$ as the pre-impact joint velocity $\dot{\boldsymbol{q}}_e^-$ of the single-stance phase to the postimpact joint velocity $\dot{\boldsymbol{q}}_e^+$ of the double-stance phase as

$$\mathcal{H}_s^d : \begin{bmatrix} \boldsymbol{D}_e(\boldsymbol{q}_e^-) & -\boldsymbol{E}_{el}^{\mathrm{T}} \\ \boldsymbol{E}_{el} & \boldsymbol{0} \end{bmatrix} \begin{bmatrix} \dot{\boldsymbol{q}}_e^+ \\ \delta\boldsymbol{F}_{el} \end{bmatrix} = \begin{bmatrix} \boldsymbol{D}_e(\boldsymbol{q}_e^-)\dot{\boldsymbol{q}}_e^- \\ \boldsymbol{0} \end{bmatrix} + \begin{bmatrix} \boldsymbol{M} \\ \boldsymbol{0}_2 \end{bmatrix} \tag{6}$$

For periodic walking gait, $\boldsymbol{M}$ can be neglected due to the insignificant input torque $\boldsymbol{u}$ applied during the impact time. However, for slip recovery process, $\boldsymbol{M}$ cannot be neglected for the intentional effort to keep balance.

The matrix on the left-hand side of Eq. (6) is invertible, and after considering the relabeling of stance foot, we have

$$\dot{\boldsymbol{q}}_a^+ = \boldsymbol{\Delta}_n(\boldsymbol{q}_e^-)\dot{\boldsymbol{q}}_e^- + \boldsymbol{b}_n \tag{7}$$

where $\boldsymbol{\Delta}_n$ is the impact mapping calculated from Eq. (6) and $\boldsymbol{b}_n$ is a constant vector that is related to $\boldsymbol{M}$. Because the new stance foot sticks to the ground, $\dot{\boldsymbol{q}}_e^+ = [(\dot{\boldsymbol{q}}_a^+)^{\mathrm{T}}\ \boldsymbol{0}_2]^{\mathrm{T}}$, and if the previous step is also nonslip, $\dot{\boldsymbol{q}}_e^- = [(\dot{\boldsymbol{q}}_a^-)^{\mathrm{T}}\ \boldsymbol{0}_2]^{\mathrm{T}}$. More detailed discussion can be found in Refs. [9] and [12].

Same as Refs. [9,13], a relabeling process is applied to the joint angles and their velocities after the impact. For the transition from the double-stance to single-stance phases, the transition is obtained as

$$\mathcal{H}_d^s : \ \boldsymbol{q}_e^+ = \boldsymbol{q}_e^-,\ \dot{\boldsymbol{q}}_e^+ = \dot{\boldsymbol{q}}_e^- \tag{8}$$

2.4 Model Optimization for Human Walking Gait. To apply the bipedal model to human gait, we need to tune the model parameters to fit the human walking data. During the human walking experiments, all joint angles and the GRF information are collected and obtained [21,22].

For single-stance dynamics (1), we need to identify and match the virtual constraint $\boldsymbol{h}(\boldsymbol{q}_a)$ in (2) from the collected joint angles. We use $\boldsymbol{H}_0 = [\boldsymbol{0}\ \boldsymbol{I}_6]$, to choose the active joints [9]. The desired trajectory $\boldsymbol{h}_d$ is parameterized by the Bézier polynomial. To fit the

double-stance model (3), we choose to optimize the Bézier spline parameters α_d such that the desired trajectory $\boldsymbol{q}_{di}^d = \boldsymbol{q}_{di}^d(\alpha_d, t)$ approximates human walking and also avoids unrealistic high joint-angular acceleration. We take the joint angular acceleration into the optimization process because the GRF matching is one of the targets besides the joint angles matched. Therefore, we minimize the following objective function:

$$J_d(\alpha_d) = \int_{t_0}^{t_f} \|\boldsymbol{q}_{di}^d(\alpha_d, t) - \boldsymbol{q}_{di}^e\|^2 + \gamma \|\ddot{\boldsymbol{q}}_{di}^d(\alpha_d, t)\|^2 dt \tag{9}$$

where $\gamma > 0$ is a weighting factor and $[t_0, t_f]$ is the time interval, and $\boldsymbol{q}_{di}^e$ is the measured joint angle profiles. By the property of the Bézier polynomials, we analytically express both $\boldsymbol{q}_{di}^d$ and $\ddot{\boldsymbol{q}}_{di}^d$ as functions of α_d, and therefore, the optimal α_d is obtained using a scaled conjugate gradient method. We will demonstrate the results in Sec. 5.

While in general it is possible to use arbitrary function to parametrize the joint angle trajectories, we specifically chose to use the Bézier polynomials, due to their wide use in modeling smooth curves that requires only few parameters particularly for biped walking model [9]. We particularly chose the fifth-order Bézier polynomials that are determined by six points. Two of these are determined as the starting and end points of the joint angle trajectory that are determined from the experiments. This simplifies the parameter estimation process. The remaining parameters are tuned based on minimizing the objective function $J_d(\alpha_d)$.

3 Bipedal Walking Model With Foot-Floor Contact Slip

In this section, we extend the bipedal model from Sec. 2 to consider the foot-floor contact slip. We first present an overview of the extended hybrid model and the detailed dynamics are then discussed.

3.1 Hybrid Model for Walking With Slip. Figure 2 shows the finite state diagram of the hybrid bipedal model for human walking with foot-floor contact slip. For the normal walking gait, the hybrid dynamics contain two states: nonslip single-stance and double-stance phases shown as $\mathcal{S}_1$ and $\mathcal{S}_2$, respectively. The heel-touch and toe-off events trigger the switching between $\mathcal{S}_1$ and $\mathcal{S}_2$ with the impact mappings $\mathcal{H}_s^d$ and $\mathcal{H}_d^s$, respectively.

The foot slip can happen during the single- and double-stance phases. Therefore, two new states are introduced for the gaits with slip: single-stance slip phase $\mathcal{S}_3$ and double-stance slip phase $\mathcal{S}_4$. State $\mathcal{S}_4$ includes the cases when slip happens on the stance leg only, the swing leg only, or both legs simultaneously. The transitions among $\mathcal{S}_1, i = 1, 2, 3, 4$, shown in Fig. 2 represent the human slip recovery strategies. For example, as we will show in the case study in Sec. 5, one slip recovery strategy can be represented in the sequence of $\mathcal{S}_1 \to \mathcal{S}_4 \to \mathcal{S}_3 \to \mathcal{S}_1$. The details of each transition in the finite state diagram are parts of the required human slip recovery strategies. These slip recovery strategies are out of the scope of this paper and we omit the discussion here.

3.2 Single-Stance Slip Model and Gait Controller. Due to foot slip, we use the extended configuration coordinate $\boldsymbol{q}_e = [\boldsymbol{q}_a^{\mathrm{T}} \ \boldsymbol{q}_s^{\mathrm{T}}]^{\mathrm{T}} = [\boldsymbol{q}_a^{\mathrm{T}} \ x_s \ y_s]^{\mathrm{T}}$ to describe the motion. The dynamic model is obtained as

$$\underbrace{\begin{bmatrix} D_{es}^{11} & D_{es}^{12} \\ D_{es}^{21} & D_{es}^{22} \\ D_{es}^{31} & D_{es}^{32} \end{bmatrix}}_{\boldsymbol{D}_{es}} \begin{bmatrix} \ddot{\boldsymbol{q}}_a \\ \ddot{x}_s \\ \ddot{y}_s \end{bmatrix} + \underbrace{\begin{bmatrix} C_{es}^{11} & C_{es}^{12} \\ C_{es}^{21} & C_{es}^{22} \\ C_{es}^{31} & C_{es}^{32} \end{bmatrix}}_{\boldsymbol{C}_{es}} \begin{bmatrix} \dot{\boldsymbol{q}}_a \\ \dot{x}_s \\ \dot{y}_s \end{bmatrix} + \underbrace{\begin{bmatrix} G_{es}^1 \\ G_{es}^2 \\ G_{es}^3 \end{bmatrix}}_{\boldsymbol{G}_{es}} = \begin{bmatrix} \boldsymbol{B}_{es}\boldsymbol{u} \\ F_x \\ F_n \end{bmatrix} = \begin{bmatrix} \boldsymbol{B}_{es}\boldsymbol{u} \\ \boldsymbol{F}_{es} \end{bmatrix} \tag{10}$$

where $\boldsymbol{D}_{es} \in \mathbb{R}^{9\times9}$, $\boldsymbol{C}_{es} \in \mathbb{R}^{9\times9}$, $\boldsymbol{G}_{es} \in \mathbb{R}^9$, and $\boldsymbol{B}_{es} \in \mathbb{R}^{7\times6}$ are the inertia, Coriolis, gravity, and input mapping matrices, respectively. We define matrices $\boldsymbol{D}_{es}^{ij}$, $\boldsymbol{C}_{es}^{ij}$, and $\boldsymbol{G}_{es}^{ij}$, where indexes $i = 1$, 2, and 3 represent, respectively, the first seven, the eighth, and the ninth row and indexes $j = 1$ and 2 represent, respectively, the first eighth and the ninth column of the matrices $\boldsymbol{D}_{es}$, $\boldsymbol{C}_{es}$, and $\boldsymbol{G}_{es}$. External force $\boldsymbol{F}_{es} = [F_x \ F_n]^{\mathrm{T}}$ is the frictional (tangential) and normal forces at the stance foot.

The stance foot is always in contact with the ground during slipping (i.e., $y_s = 0$), and therefore, we have constraint $\boldsymbol{q}_s = [x_s \ y_s]^{\mathrm{T}} = [x_s \ 0]^{\mathrm{T}}$. Also, we have $F_x = -\mu F_n$, where μ is the friction coefficient between the shoe sole and the ground floor. With these constraints, we further simplify Eq. (10) by defining new coordinate $\boldsymbol{q}_{es} = [\boldsymbol{q}_a \ x_s]^{\mathrm{T}} \in \mathbb{R}^8$ and eliminating external force F_n and finally obtain

$$\boldsymbol{\Sigma}_s^s : \boldsymbol{D}_{es}^s \ddot{\boldsymbol{q}}_{es} + \boldsymbol{C}_{es}^s \dot{\boldsymbol{q}}_{es} + \boldsymbol{G}_{es}^s = \boldsymbol{B}_{es}^s \boldsymbol{u} \tag{11}$$

where

$$\boldsymbol{D}_{es}^s = \begin{bmatrix} \boldsymbol{D}_{es}^{11} \\ \boldsymbol{D}_{es}^{21} + \mu \boldsymbol{D}_{es}^{31} \end{bmatrix}, \quad \boldsymbol{C}_{es}^s = \begin{bmatrix} \boldsymbol{C}_{es}^{11} \\ \boldsymbol{C}_{es}^{21} + \mu \boldsymbol{C}_{es}^{31} \end{bmatrix} \in \mathbb{R}^{8\times8},$$

$$\boldsymbol{G}_{es}^s = \begin{bmatrix} \boldsymbol{G}_{es}^1 \\ G_{es}^2 + \mu G_{es}^3 \end{bmatrix} \in \mathbb{R}^8, \quad \boldsymbol{B}_{es}^s = \begin{bmatrix} \boldsymbol{B}_{es} \\ 0 \end{bmatrix} \in \mathbb{R}^{8\times6}$$

The system given by Eq. (11) has eight state variables and six joint torques as inputs, and therefore, it is underactuated. The absolute joint angle q_1 and the slipping distance x_s are underactuated variables. To use model (11) for human gait prediction, we adopt a similar controller as for the nonslip case. A six-dimensional holonomic virtual constraint $\boldsymbol{y} = \boldsymbol{h}(\boldsymbol{q}_a) = \boldsymbol{H}_0 \boldsymbol{q}_a - \boldsymbol{h}_d(\theta_s)$ is used to design the control system, where $\theta_s = \boldsymbol{c}_s \boldsymbol{q}_a$ and $\boldsymbol{c}_s$ is chosen to ensure $[\boldsymbol{H}_0^{\mathrm{T}} \ \boldsymbol{c}_s^{\mathrm{T}}]^{\mathrm{T}}$ is full rank. Similar to the nonslip case, letting $\boldsymbol{\eta} = \boldsymbol{h}(\boldsymbol{q}_a)$, the control $\boldsymbol{u}$ is chosen to regulate $\boldsymbol{\eta} = \dot{\boldsymbol{\eta}} = 0$ and the zero dynamics are obtained. Specifically, we define $\xi = (\boldsymbol{D}_{es}^{11})_1 \dot{\boldsymbol{q}}_a$, where $(\boldsymbol{D}_{es}^{11})_1$ is the first seven elements of the first row of matrix $\boldsymbol{D}_{es}^{11}$ and it corresponds to the unactuated variable q_1. The dynamics of ξ and $\dot{x}_s$ are indeed the zero dynamics of the system and will be presented in Sec. 4. Compared with the nonslip single-stance case, the zero dynamics of the slip walking model contain one additional variable $\dot{x}_s$.

3.3 Double-Stance Slip Model and Gait Controller. During the double-stance slip gait, either (i) only one of two feet slips while the other foot purely rolls on the ground, or (ii) both feet slide on the ground. These two situations share the same equations of motion given by Eq. (3) but with different governing constraints. For the first case, we always define the nonslipping leg as the stance leg, and from the stance leg, we define the absolute joint angle q_1; see Fig. 1(*a*). For the second case, we take either leg as the stance leg.

By such arrangements, for case (i), without loss of generality, we assume that the trailing leg is nonslip and also the stance leg. Therefore, we have kinematic constraints $\boldsymbol{g}_t(\boldsymbol{q}_e) = \boldsymbol{0}$ and $(\boldsymbol{g}_l(\boldsymbol{q}_e))_y = 0$, where $(\boldsymbol{g}_i(\boldsymbol{q}_e))_j$, $i = l, t$, $j = x, y$, represents the jth coordinate of slipping vector $\boldsymbol{g}_i(\boldsymbol{q}_e)$. Moreover, we have the kinetic constraints $F_{xl} = -\mu F_{nl}$ for slipping foot. Similarly, for case (ii), we have the kinematic constraints $(\boldsymbol{g}_t(\boldsymbol{q}_e))_y = (\boldsymbol{g}_l(\boldsymbol{q}_e))_y = 0$ and the kinetic constraints $F_{xt} = -\mu F_{nt}$ and $F_{xl} = -\mu F_{nl}$. In the following, we only present the dynamics for case (i) and similar results can be obtained for case (ii).

Because of constraints $\boldsymbol{g}_t(\boldsymbol{q}_e) = \boldsymbol{0}$ and $(\boldsymbol{g}_l(\boldsymbol{q}_e))_y = 0$, we obtain $(\partial \boldsymbol{g}_t / \partial \boldsymbol{q}_e)\dot{\boldsymbol{q}}_e = \boldsymbol{0}$ and $(\partial (\boldsymbol{g}_l(\boldsymbol{q}_e))_y / \partial \boldsymbol{q}_e)\dot{\boldsymbol{q}}_e = 0$. Using the definition of $\boldsymbol{E}_e$ in Eq. (3), these kinematic constraints are written into compact form $\boldsymbol{E}_{es}\dot{\boldsymbol{q}}_e = \boldsymbol{0}$, where $\boldsymbol{E}_{es} := (\boldsymbol{E}_e)_{[1,2,4]} \in \mathbb{R}^{3\times9}$ is a matrix formed by taking rows 1, 2, and 4 of $\boldsymbol{E}_e$. Similarly, the

kinetic constraint $F_{xl} = -\mu F_{nl}$ is used to rewrite the external force vector in Eq. (3) as

$$\boldsymbol{F}_e = \underbrace{\begin{bmatrix} 1 & 0 & 0 \\ 0 & 1 & 0 \\ 0 & 0 & -\mu \\ 0 & 0 & 1 \end{bmatrix}}_{\boldsymbol{C}_f} \underbrace{\begin{bmatrix} F_{xt} \\ F_{nt} \\ F_{nl} \end{bmatrix}}_{\boldsymbol{F}_{e3}} = \boldsymbol{C}_f \boldsymbol{F}_{e3} \tag{12}$$

Similar to the treatment to obtain Eq. (5), by taking derivative of velocity constraint $\boldsymbol{E}_{es}\dot{\boldsymbol{q}}_e = \boldsymbol{0}$ and stacking with the simplified Eqs. (3) and (12), we obtain

$$\underbrace{\begin{bmatrix} \boldsymbol{D}_e & -\boldsymbol{E}_e^{\mathrm{T}}\boldsymbol{C}_f \\ \boldsymbol{E}_{es} & \boldsymbol{0} \end{bmatrix}}_{\boldsymbol{D}^s_{\mathrm{ext}}} \begin{bmatrix} \ddot{\boldsymbol{q}}_e \\ \boldsymbol{F}_{e3} \end{bmatrix} = \underbrace{\begin{bmatrix} \boldsymbol{B}_e \\ \boldsymbol{0} \end{bmatrix}}_{\boldsymbol{B}^s_{\mathrm{ext}}} \boldsymbol{u} - \underbrace{\begin{bmatrix} \boldsymbol{C}_e \\ \dot{\boldsymbol{E}}_{es} \end{bmatrix} \dot{\boldsymbol{q}}_e - \begin{bmatrix} \boldsymbol{G}_e \\ \boldsymbol{0} \end{bmatrix}}_{\boldsymbol{C}^s_{\mathrm{ext}}}$$

Matrix $\boldsymbol{D}^s_{\mathrm{ext}}$ is full rank, and therefore, $\ddot{\boldsymbol{q}}_e$ and $\boldsymbol{F}_{e3}$ are uniquely determined once the current state variables and joint torques $\boldsymbol{u}$ are given. Since the three-dimensional constraints $\boldsymbol{E}_{es}\dot{\boldsymbol{q}}_e = \boldsymbol{0}$ are enforced, the degrees-of-freedom of the system are $9 - 3 = 6$. Therefore, the system is fully actuated.

Letting $\boldsymbol{q}_i = [q_1\ q_2\ q_3\ q_4\ q_5\ q_7]^{\mathrm{T}} = \boldsymbol{S}\boldsymbol{q}_e$ be the independent variables, where $\boldsymbol{S} \in \mathbb{R}^{6\times 9}$ is a constant transformation matrix from $\boldsymbol{q}_e$ to $\boldsymbol{q}_i$, we express $\ddot{\boldsymbol{q}}_i = \boldsymbol{S}(\boldsymbol{D}^s_{\mathrm{ext}}{}^{-1}\boldsymbol{B}^s_{\mathrm{ext}}\boldsymbol{u} + \boldsymbol{D}^s_{\mathrm{ext}}{}^{-1}\boldsymbol{C}^s_{\mathrm{ext}})$, where $\boldsymbol{S}\boldsymbol{D}^s_{\mathrm{ext}}{}^{-1}\boldsymbol{B}^s_{\mathrm{ext}} \in \mathbb{R}^{6\times 6}$ is a full rank matrix. To track a given trajectory $\boldsymbol{q}_i^d$, the controlled joint torque is designed as $\boldsymbol{u} = (\boldsymbol{S}\boldsymbol{D}^s_{\mathrm{ext}}{}^{-1}\boldsymbol{B}^s_{\mathrm{ext}})^{-1}(\ddot{\boldsymbol{q}}_i^d - \boldsymbol{K}_p(\boldsymbol{q}_i - \boldsymbol{q}_i^d) - \boldsymbol{K}_d(\dot{\boldsymbol{q}}_i - \dot{\boldsymbol{q}}_i^d) - \boldsymbol{S}\boldsymbol{D}^s_{\mathrm{ext}}{}^{-1}\boldsymbol{C}^s_{\mathrm{ext}})$, where $\boldsymbol{K}_p$ and $\boldsymbol{K}_d$ are constant gain matrices.

3.4 Impact Model for Walking Gait With Slip. The impact model under slip is obtained from the extension of the nonslip case in Sec. 2.3. The main difference is that the slip can happen right after the impact, and therefore, the velocity of heel-touch contact point C_l is possibly nonzero, unlike zero in nonslip case. From the discussion in Sec. 3.3, we have the velocity constraint $\boldsymbol{E}_e\dot{\boldsymbol{q}}_e = \boldsymbol{v}_{\mathrm{slip}} = [\boldsymbol{0}\ \boldsymbol{0}\ v_{\mathrm{slip}}\ \boldsymbol{0}]^{\mathrm{T}}$, where v_{slip} is the slipping velocity of point C_l (along the x-axis direction) after the heel-touch impact. Therefore, we obtain

$$\mathcal{H}^s_n: \begin{bmatrix} \boldsymbol{D}_e(\boldsymbol{q}_e^-) & -\boldsymbol{E}_e^{\mathrm{T}} \\ \boldsymbol{E}_e & \boldsymbol{0} \end{bmatrix} \begin{bmatrix} \dot{\boldsymbol{q}}_e^+ \\ \delta\boldsymbol{F}_e \end{bmatrix} = \begin{bmatrix} \boldsymbol{D}_e(\boldsymbol{q}_e^-)\dot{\boldsymbol{q}}_e^- \\ \boldsymbol{v}_{\mathrm{slip}} \end{bmatrix} \tag{13}$$

Compared with Eq. (6), one more unknown $\dot{x}_s^+$ is introduced. We here use the friction coefficient to relate impulses $F_{2x} = -\mu F_{2y}$ because of the friction model and the integration over instantaneous impact time. Considering relabeling, we have

$$\dot{\boldsymbol{q}}_e^+ = \begin{bmatrix} \dot{\boldsymbol{q}}_a^+ \\ \dot{x}_s^+ \\ \boldsymbol{0} \end{bmatrix} = \boldsymbol{\Delta}_s(\boldsymbol{q}_e^-)\dot{\boldsymbol{q}}_e^- \tag{14}$$

where $\boldsymbol{\Delta}_s$ denotes the foot-slip impact mapping matrix.

4 Hybrid Zero Dynamics of Slip Recovery

In this section, we first present the HZD for bipedal walking with foot slip. Then, we discuss a set of slip recovery phases that are observed in the experiments. Finally, we introduce the stability of slip recovery sequence. Since single-stance phase takes main stance gait duration, and due to the complexity of the double-stance dynamics, only single-stance dynamics are considered in the HZD analysis. This simplification helps highlight the HZD of slip recovery process in later discussion, and also allows us to consider only the continuous nonslip and slip dynamics, $\mathcal{S}_1$ and $\mathcal{S}_3$, and their respective impact mapping transitions. For completeness, two additional return impact mappings are required: $\mathcal{H}^n_n$ and $\mathcal{H}^s_s$ transitions back to the nonslip single-stance phase ($\mathcal{S}_1$) and the slip single-stance ($\mathcal{S}_3$), respectively. These are all defined in domain π_{HZD} as shown in Fig. 2.

4.1 Zero Dynamics of Nonslip Single-Stance Phase. The nonslip single-stance zero dynamics is obtained by enforcing the states of Eq. (1) onto the virtual constraint (2). Following a similar treatment in Ref. [12], we define $\boldsymbol{x}_a = [\boldsymbol{q}_a^{\mathrm{T}}\ \dot{\boldsymbol{q}}_a^{\mathrm{T}}]^{\mathrm{T}}$ and rewrite (1) into a first-order form

$$\dot{\boldsymbol{x}}_a = \boldsymbol{f}(\boldsymbol{x}_a) + \boldsymbol{g}(\boldsymbol{x}_a)\boldsymbol{u} \tag{15}$$

where $\boldsymbol{f}(\boldsymbol{x}_a) = \begin{bmatrix} \dot{\boldsymbol{q}}_a \\ -\boldsymbol{D}_s^{-1}(\boldsymbol{C}_s\dot{\boldsymbol{q}}_a + \boldsymbol{G}_s) \end{bmatrix}$, $\boldsymbol{g}(\boldsymbol{x}_a) = \begin{bmatrix} \boldsymbol{0}_{7\times 6} \\ \boldsymbol{D}_s^{-1}\boldsymbol{B}_s \end{bmatrix}$. We consider a coordinate transformation

$$\boldsymbol{\eta}_1 = \boldsymbol{h}(\boldsymbol{q}_a), \quad \boldsymbol{\eta}_2 = L_f\boldsymbol{h}(\boldsymbol{q}_a), \quad \xi_1 = \theta(\boldsymbol{q}_a), \quad \xi_2 = \boldsymbol{D}_a(\boldsymbol{q}_a)\dot{\boldsymbol{q}}_a \tag{16}$$

where $L_f\boldsymbol{h}(\boldsymbol{q}_a)$ is the Lie derivative of $\boldsymbol{h}(\boldsymbol{q}_a)$ along $\boldsymbol{f}$, and $\boldsymbol{D}_a(\boldsymbol{q})$ is formed by the row of $\boldsymbol{D}_s(\boldsymbol{q})$ that corresponds to the unactuated joint angle q_1. Choosing $\boldsymbol{u} = (L_{\boldsymbol{g}}L_f\boldsymbol{h})^{-1}(-L_f^2\boldsymbol{h} + \boldsymbol{v})$ and $\boldsymbol{v}$ to regulate $\boldsymbol{\eta}_1 = \boldsymbol{\eta}_2 = \boldsymbol{0}$ exponentially, the output dynamics become $\dot{\boldsymbol{\eta}}_1 = \boldsymbol{\eta}_2$, $\dot{\boldsymbol{\eta}}_2 = \boldsymbol{v}$. The zero dynamics is given as

$$\boldsymbol{\Sigma}^n_{ZD}: \begin{cases} \dot{\xi}_1 = \dfrac{\partial\theta}{\partial\boldsymbol{q}_a}\dot{\boldsymbol{q}}_a =: k_1(\xi_1)\xi_2, \\ \dot{\xi}_2 = \dot{\boldsymbol{q}}_a^{\mathrm{T}}\dfrac{\partial\boldsymbol{D}_a^{\mathrm{T}}}{\partial\boldsymbol{q}_a}\dot{\boldsymbol{q}}_a - \boldsymbol{C}_a\dot{\boldsymbol{q}}_a - \boldsymbol{G}_a =: k_2(\xi_1, \xi_2) \end{cases} \tag{17}$$

The transformation of output $\boldsymbol{\eta} := [\boldsymbol{\eta}_1^{\mathrm{T}}\ \boldsymbol{\eta}_2^{\mathrm{T}}]^{\mathrm{T}}$ and internal states $\boldsymbol{\xi} := [\xi_1\ \xi_2]^{\mathrm{T}}$ to $\boldsymbol{x}_a$ is obtained as

$$\begin{bmatrix} \boldsymbol{\eta}_1 \\ \xi_1 \end{bmatrix} = \begin{bmatrix} \boldsymbol{h}(\boldsymbol{q}_a) \\ \theta(\boldsymbol{q}_a) \end{bmatrix} =: \boldsymbol{\Phi}(\boldsymbol{q}_a), \quad \begin{bmatrix} \boldsymbol{\eta}_2 \\ \xi_2 \end{bmatrix} = \begin{bmatrix} \dfrac{\partial\boldsymbol{h}(\boldsymbol{q}_a)}{\partial\boldsymbol{q}_a} \\ \boldsymbol{D}_a(\boldsymbol{q}_a) \end{bmatrix}\dot{\boldsymbol{q}}_a \tag{18}$$

and the inverse transformation is

$$\boldsymbol{q}_a = \boldsymbol{\Phi}^{-1}\left(\begin{bmatrix} \boldsymbol{\eta}_1 \\ \xi_1 \end{bmatrix}\right), \quad \dot{\boldsymbol{q}}_a = \begin{bmatrix} \dfrac{\partial\boldsymbol{h}(\boldsymbol{q}_a)}{\partial\boldsymbol{q}_a} \\ \boldsymbol{D}_a(\boldsymbol{q}_a) \end{bmatrix}^{-1}\begin{bmatrix} \boldsymbol{\eta}_2 \\ \xi_2 \end{bmatrix} \tag{19}$$

When $\boldsymbol{\eta} = \boldsymbol{0}$, $\boldsymbol{x}_a$ is a function of only $\boldsymbol{\xi}$ and the right-hand side of Eq. (17) can be written as a function of $\boldsymbol{\xi}$.

To maintain stable gaits, the pre-impact states should be mapped to zero dynamics space under the impact mapping (7) [9], that is

$$\boldsymbol{\Delta}_n(\boldsymbol{S} \cap \boldsymbol{Z}_{\alpha_n}) \subset \boldsymbol{Z}_{\alpha_n} \tag{20}$$

where $\boldsymbol{S}$ is the double-stance configuration space and $\boldsymbol{Z}_{\alpha_n}$ is the single-stance zero dynamics space under normal walking gait profile α_n. Assuming the pre-impact zero dynamics state is $\boldsymbol{\xi}^-$, the pre-impact full state is $\boldsymbol{x}_a^-$ by applying Eq. (19) with $\boldsymbol{\eta} = \boldsymbol{0}$. The postimpact state is obtained $\boldsymbol{x}_a^+$ by Eq. (7). The hybrid invariant set requires that the after-impact state is still on the zero dynamic space, namely

$$\boldsymbol{\eta}_1 = \boldsymbol{h}(\boldsymbol{q}_a^+) = \boldsymbol{0}, \quad \boldsymbol{\eta}_2 = \frac{\partial\boldsymbol{h}}{\partial\boldsymbol{q}_a}(\boldsymbol{q}_a^+)\dot{\boldsymbol{q}}_a^+ = \boldsymbol{0}$$

4.2 Zero Dynamics of Single-Stance Phase With Slip. The slip single-stance phase dynamics (11) has 2 deg of underactuation,

i.e., the absolute joint angle q_1 and the slip distance x_s. The six dimension virtual constraint for slip single-stance phase is

$$\boldsymbol{y} = \boldsymbol{h}_s(\boldsymbol{q}_a) = \boldsymbol{0} \tag{21}$$

Similar to the nonslip case, defining $\boldsymbol{x}_{es} = \left[\boldsymbol{q}_{es}^{\mathrm{T}} \;\; \dot{\boldsymbol{q}}_{es}^{\mathrm{T}}\right]^{\mathrm{T}}$, Eq. (11) is written as

$$\dot{\boldsymbol{x}}_{es} = \boldsymbol{f}_s(\boldsymbol{x}_{es}) + \boldsymbol{g}_s(\boldsymbol{x}_{es})\boldsymbol{u} \tag{22}$$

where $\boldsymbol{f}_s$ and $\boldsymbol{g}_s$ are similar to those in Eq. (15) with corresponding coefficient matrices from $\boldsymbol{\Sigma}_s$ in Eq. (11). Defining the state transformation $\boldsymbol{\eta}_s = \left[\boldsymbol{\eta}_{1s}^{\mathrm{T}} \;\; \boldsymbol{\eta}_{2s}^{\mathrm{T}}\right]^{\mathrm{T}} = \left[\boldsymbol{h}_s(q_a) \; L_{f_s}\boldsymbol{h}_s\right]^{\mathrm{T}}$, we use the feedback linearization to obtain the output dynamics $\dot{\boldsymbol{\eta}}_{1s} = \boldsymbol{\eta}_{2s}$, $\dot{\boldsymbol{\eta}}_{2s} = \boldsymbol{w}$, where $\boldsymbol{w}$ is the new control input to drive $\boldsymbol{\eta}_s$ to zero exponentially. The zero dynamics states are defined as

$$\xi_{1s} = \theta_s(\boldsymbol{q}_a), \quad \xi_{2s} = \boldsymbol{D}_{esq}^s \dot{\boldsymbol{q}}_{es}, \quad x_{1s} = x_s, \quad x_{2s} = \boldsymbol{D}_{esx}^s \dot{\boldsymbol{q}}_{es} \tag{23}$$

where $\boldsymbol{D}_{esq}^s$ and $\boldsymbol{D}_{esx}^s$ are the rows in $\boldsymbol{D}_{es}^s$ that correspond to the unactuated angle q_1 and slip distance x_s, respectively. Note that $\boldsymbol{D}_{es}^s$ does not depend on x_s.

Similar to Eq. (18), we obtain the transformation between the new coordinates $\boldsymbol{\eta}_s$, $\boldsymbol{\xi}_s$, and $\boldsymbol{x}_s = [x_{1s} \;\; x_{2s}]^{\mathrm{T}}$ with the original states $\boldsymbol{x}_{es}$ as

$$\begin{bmatrix} \boldsymbol{\eta}_{1s} \\ \xi_{1s} \\ x_{1s} \end{bmatrix} = \begin{bmatrix} \boldsymbol{\Phi}_s(\boldsymbol{q}_a) \\ x_s \end{bmatrix}, \quad \begin{bmatrix} \boldsymbol{\eta}_{2s} \\ \xi_{2s} \\ x_{2s} \end{bmatrix} = \underbrace{\begin{bmatrix} \frac{\partial \boldsymbol{h}_s}{\partial \boldsymbol{q}_a} & \boldsymbol{0} \\ \boldsymbol{D}_{esq}^s(\boldsymbol{q}_a) & \\ \boldsymbol{D}_{esx}^s(\boldsymbol{q}_a) & \end{bmatrix}}_{\boldsymbol{\lambda}(\boldsymbol{q}_a)} \dot{\boldsymbol{q}}_{es} = \boldsymbol{\lambda}(\boldsymbol{q}_a)\dot{\boldsymbol{q}}_{es}$$

where $\boldsymbol{\Phi}_s(\boldsymbol{q}_a) = [\boldsymbol{h}_s \; \theta_s]^{\mathrm{T}} = \left[\boldsymbol{\eta}_{1s}^{\mathrm{T}} \;\; \xi_{1s}\right]^{\mathrm{T}}$ and the inverse transformation is

$$\boldsymbol{q}_{es} = \begin{bmatrix} \boldsymbol{q}_a \\ x_s \end{bmatrix} = \begin{bmatrix} \boldsymbol{\Phi}_s^{-1} \\ x_{1s} \end{bmatrix}, \quad \dot{\boldsymbol{q}}_{es} = \boldsymbol{\lambda}^{-1}(\boldsymbol{q}_a) \begin{bmatrix} \boldsymbol{\eta}_{2s} \\ \xi_{2s} \\ x_{2s} \end{bmatrix} \tag{24}$$

The zero dynamics is given as

$$\begin{aligned} \dot{\xi}_{1s} &= \frac{\partial \theta_s}{\partial \boldsymbol{q}_a}\dot{\boldsymbol{q}}_a, \quad \dot{x}_{1s} = \dot{x}_s, \\ \dot{\xi}_{2s} &= \dot{\boldsymbol{q}}_{es}^{\mathrm{T}} \frac{\partial (\boldsymbol{D}_{esq}^s)^{\mathrm{T}}}{\partial \boldsymbol{q}_{es}} \dot{\boldsymbol{q}}_{es} - \boldsymbol{C}_{esq}^s \dot{\boldsymbol{q}}_s - \boldsymbol{G}_{esq}^s =: k_{2s}(\xi_{1s}, \xi_{2s}, x_{2s}), \\ \dot{x}_{2s} &= \dot{\boldsymbol{q}}_{es}^{\mathrm{T}} \frac{\partial (\boldsymbol{D}_{esx}^s)^{\mathrm{T}}}{\partial \boldsymbol{q}_s} \dot{\boldsymbol{q}}_s - \boldsymbol{C}_{esx}^s \dot{\boldsymbol{q}}_s - \boldsymbol{G}_{esx}^s \end{aligned} \tag{25}$$

From the property of robot motion (10) [26], we obtain

$$\boldsymbol{C}_{esx}^s = \dot{\boldsymbol{q}}_s^{\mathrm{T}} \frac{\partial (\boldsymbol{D}_{esx}^s)^{\mathrm{T}}}{\partial \boldsymbol{q}_s} \tag{26}$$

We simplify the zero dynamics by substituting Eq. (26) into Eq. (25) with Eq. (24) and $\boldsymbol{\eta}_s = \boldsymbol{0}$, and obtain

$$\begin{bmatrix} \dot{\xi}_{1s} \\ \dot{x}_{1s} \end{bmatrix} = \begin{bmatrix} \frac{\partial \theta_s}{\partial \boldsymbol{q}_a} & \boldsymbol{0} \\ \boldsymbol{0}_N^T & 1 \end{bmatrix} \boldsymbol{\lambda}^{-1}(\boldsymbol{q}_a) \begin{bmatrix} \boldsymbol{0}_{N-1} \\ \xi_{2s} \\ x_{2s} \end{bmatrix} =: \boldsymbol{k}_{1s}(\xi_{1s}) \begin{bmatrix} \xi_{2s} \\ x_{2s} \end{bmatrix},$$
$$\dot{\xi}_{2s} = k_{2s}(\xi_{1s}, \xi_{2s}, x_{2s}), \quad \dot{x}_{2s} = -\boldsymbol{G}_{esx}^s =: k_{3s}(\xi_{1s}) \tag{27}$$

where $\boldsymbol{k}_{1s}(\xi_{1s})$ and $k_{3s}(\xi_{1s})$ are defined as the coefficients in the above equations.

4.3 Multistep Slip Recovery Process and Stability. A slip recovery process can be considered a series of walking gaits. We here use a recovery gait sequence as an example to illustrate the principles and stability of the recovery process, and the results can be extended to other gait sequences.

As shown in Fig. 2, considering π_{HZD}, the normal walking dynamics are described by nonslip continuous dynamics $\mathcal{S}_1$ and transition through nonslip foot impact $\mathcal{H}_n^n$. The normal gait profile (virtual constraints) is denoted by α_n. When slip happens, phase $\mathcal{S}_1$ with gait α_n transits through the slip impact $\mathcal{H}_n^s$ to slip single-stance phase $\mathcal{S}_3$. In $\mathcal{S}_3$, human tries to touch down the swing foot as soon as possible to find the new support and the gait is described as α_s. Once the swing foot touches down, phase $\mathcal{S}_3$ transits back to phase $\mathcal{S}_1$ through impact $\mathcal{H}_s^n$. A recovery gait profile α_r is adopted during this phase. Finally, the gait is successfully recovered back to $\mathcal{S}_1$ with gait profile α_n. From the above description, the slip recovery process is summarized as

$$\mathcal{S}_1(\alpha_n) \xrightarrow{\mathcal{H}_n^s} \mathcal{S}_3(\alpha_s) \xrightarrow{\mathcal{H}_n^s} \mathcal{S}_1(\alpha_r) \xrightarrow{\mathcal{H}_n^s} \mathcal{S}_1(\alpha_n) \tag{28}$$

Note from Fig. 2 that a stable cyclic gait exists for single-stance slip phase $\mathcal{S}_3$ with gait profile α_s and impact $\mathcal{H}_s^s$. This gait does not happen usually in human walking locomotion because it requires skills to regulate highly dynamic motion under foot slip. One example for such gaits is used in figure skating skills in which both stepping and foot slipping co-exist for stable gaits. To demonstrate the capabilities of the extended HZD, we present the results of skating motion later in Sec. 5.

The nonslip or slip single-stance zero dynamics controllers only drive the system states onto the zero dynamics space of certain phase. To build a zero dynamics space covering the entire slip recovery process, it is necessary to guarantee that the zero dynamics space is invariant under slip ($\mathcal{H}_n^s$) and recovery impacts ($\mathcal{H}_s^n$). Similar to Eq. (20), the following conditions should be satisfied for the recovery sequence in Eq. (28):

$$\boldsymbol{\Delta}_s(\boldsymbol{S} \cap \boldsymbol{Z}_{\alpha_n}) \subset \boldsymbol{Z}_{\alpha_s}, \quad \boldsymbol{\Delta}_n(\boldsymbol{S} \cap \boldsymbol{Z}_{\alpha_s}) \subset \boldsymbol{Z}_{\alpha_r}, \quad \boldsymbol{\Delta}_n(\boldsymbol{S} \cap \boldsymbol{Z}_{\alpha_r}) \subset \boldsymbol{Z}_{\alpha_n} \tag{29}$$

where $\boldsymbol{Z}_{\alpha_s}$ and $\boldsymbol{Z}_{\alpha_r}$ are the slipping and recover step zero dynamics spaces, respectively.

Assuming pre-impact zero dynamics state under a normal walking gait α_n is given as $\boldsymbol{\xi}^- \in \boldsymbol{S} \cap \boldsymbol{Z}_{\alpha_n}$, the pre-impact full state is then $\boldsymbol{x}_a(\boldsymbol{\xi}^-)$ by applying Eq. (19) with $\boldsymbol{\eta} = \boldsymbol{0}$. After the slip impact (14), the initial full state of slip swing phase is $\boldsymbol{x_{es}}^+(\boldsymbol{\xi}^-)$. Condition (29) requires that $\boldsymbol{\eta}_{1s}(\boldsymbol{x_{es}^+}) = \boldsymbol{h}_{\alpha_s}(\boldsymbol{q_{es}^+}) = \boldsymbol{0}$ and $\boldsymbol{\eta}_{2s}(\boldsymbol{x_{es}^+}) = (\partial \boldsymbol{h}_{\alpha_s}/\partial \boldsymbol{q}_a)(\boldsymbol{q_{es}^+})\dot{\boldsymbol{q}}_{es}^+ = \boldsymbol{0}$. Meanwhile, in the HZD space, after the impact, $\left[\boldsymbol{\xi}_s^+ \; \boldsymbol{x}_s^+\right]^{\mathrm{T}} \in \boldsymbol{Z}_{\alpha_s}$ is related to the pre-impact state $\boldsymbol{\xi}^- \in \boldsymbol{S} \cap \boldsymbol{Z}_{\alpha_n}$ as

$$\begin{bmatrix} \boldsymbol{\xi}_s^+ \\ \boldsymbol{x}_s^+ \end{bmatrix} = \begin{bmatrix} \theta_s(\boldsymbol{q}_a^+) \\ \boldsymbol{D}_{esq}^s(\boldsymbol{q}_a^+)\dot{\boldsymbol{q}}_{es}^+ \\ x_s^+ \\ \boldsymbol{D}_{esx}^s(\boldsymbol{q}_a^+)\dot{\boldsymbol{q}}_{es}^+ \end{bmatrix} = \begin{bmatrix} \theta_s(\boldsymbol{T}\boldsymbol{q}_a(\xi_1^-)) \\ \boldsymbol{D}_{esq}^s(\boldsymbol{T}\boldsymbol{q}_a(\xi_1^-))\Delta_s \dot{\boldsymbol{q}}_a(\xi_2^-) \\ 0 \\ \boldsymbol{D}_{esx}^s(\boldsymbol{T}\boldsymbol{q}_a(\xi_1^-))\Delta_s \dot{\boldsymbol{q}}_a(\xi_2^-) \end{bmatrix} =: \boldsymbol{\delta}_n^s(\boldsymbol{\xi}^-) \tag{30}$$

where $\boldsymbol{T}$ is the relabel matrix and the above equation is obtained by applying Eqs. (14), (19), and (23).

To compute the ending state in the slip single-stance phase, we integrate Eq. (27) with respect to time, until either $\xi_{1s} = \xi_{1s}^+$ (start of the step) or $\xi_{1s} = \xi_{1s}^-$ (ending of the step), which implies, respectively, either not being able to complete this step and return to the initial configuration of this phase, or a complete step is achieved. We denote the ending state as

$$\begin{bmatrix} \xi_{2s}^- \\ \boldsymbol{x}_s^- \end{bmatrix} = \boldsymbol{\Psi}_s\left(\boldsymbol{\xi}^+, \boldsymbol{x}_s^+; t_s\right) \tag{31}$$

where $\boldsymbol{\Psi}_s(\boldsymbol{\xi}_0, \boldsymbol{x}_0; t)$ represents the solution (flow) of the zero dynamics (27) from initial condition $(\boldsymbol{\xi}_0, \boldsymbol{x}_0)$ at $t = 0$ to $(\boldsymbol{\xi}_s^-, \boldsymbol{x}_s^-)$ at $t = t_s$. At the end of slip single-stance phase, the swing foot impacts on the ground and the slipping foot lifts immediately. The pre-impact zero dynamic state is $[\boldsymbol{\xi}_s^-, \boldsymbol{x}_s^-]^{\mathrm{T}} \in \boldsymbol{S} \cap \boldsymbol{Z}_{\alpha_s}$. The full state is $\boldsymbol{x}_{es}(\boldsymbol{\xi}_s^-, \boldsymbol{x}_s^-)$ according to Eq. (24) under condition $\boldsymbol{\eta}_s = \boldsymbol{0}$. After the stick impact, the initial state of recovery step is $\boldsymbol{x}_a^+$ from Eq. (7). Condition (29) requires that $\boldsymbol{\eta}_1 = \boldsymbol{h}_{\alpha_r}(\boldsymbol{q}_a^+) = \boldsymbol{0}$ and $\boldsymbol{\eta}_2 = (\partial \boldsymbol{h}_{\alpha_r}/\partial \boldsymbol{q}_a)(\boldsymbol{q}_a^+)\dot{\boldsymbol{q}}_a^+ = \boldsymbol{0}$.[3]

The initial HZD state of the recovery step swing phase $\boldsymbol{\xi}^+ \in \boldsymbol{Z}_{\alpha_r}$ is related to the pre-impact state $[\boldsymbol{\xi}_s^-, \boldsymbol{x}_s^-]^{\mathrm{T}} \in \boldsymbol{S} \cap \boldsymbol{Z}_{\alpha_s}$ as

$$\boldsymbol{\xi}^+ = \begin{bmatrix} \theta\left(\boldsymbol{T}\boldsymbol{q}_a\left(\xi_{1s}^-\right)\right) \\ \boldsymbol{D}_a\left(\boldsymbol{T}\boldsymbol{q}_a\left(\xi_{1s}^-\right)\right)\left(\Delta_n \dot{\boldsymbol{q}}_a\left(\boldsymbol{\xi}_s^-, \boldsymbol{x}_s^-\right) + \boldsymbol{b}_n\right) \end{bmatrix} =: \boldsymbol{\delta}_s^n\left(\boldsymbol{\xi}_s^-, \boldsymbol{x}_s^-\right) \tag{32}$$

where Eqs. (7), (16), and (24) are used to obtain the above equation. The continuous recovery zero dynamics is described by Eq. (17). We solve Eq. (17) with respect to time until either $\xi_1 = \xi_1^+$ or $\xi_1 = \xi_1^-$, which indicates either not being able to complete this recovery step and returning to the initial configuration of this phase, or a complete recovery step is achieved, respectively. We denote the ending state as $\xi_2^- = \Phi_{\alpha_r}(\boldsymbol{\xi}^+)$.

At the end of recovery step, the HZD state is $\boldsymbol{\xi}^- \in \boldsymbol{S} \cap \boldsymbol{Z}_{\alpha_r}$ and the full state is $\boldsymbol{x}_a(\boldsymbol{\xi}^-)$. After the impact, the initial state is $\boldsymbol{x}_a^+$ from Eq. (7). Condition (29) requires that $\boldsymbol{\eta}_1 = \boldsymbol{h}_{\alpha_n}(\boldsymbol{q}_a^+) = 0$ and $\boldsymbol{\eta}_2 = (\partial \boldsymbol{h}_{\alpha_n}/\partial \boldsymbol{q}_a)(\boldsymbol{q}_a^+)\dot{\boldsymbol{q}}_a^+ = \boldsymbol{0}$. Meanwhile, state $\boldsymbol{\xi}^+ \in \boldsymbol{Z}_{\alpha_n}$ is related to pre-impact state $\boldsymbol{\xi}^- \in \boldsymbol{S} \cap \boldsymbol{Z}_{\alpha_r}$ as

$$\boldsymbol{\xi}^+ = \begin{bmatrix} \theta(\boldsymbol{T}\boldsymbol{q}_a(\xi_1^-)) \\ \boldsymbol{D}_a(\boldsymbol{T}\boldsymbol{q}_a(\xi_1^-))\left(\boldsymbol{\Lambda}_n \dot{\boldsymbol{q}}_a(\boldsymbol{\xi}^-) + \boldsymbol{b}_n\right) \end{bmatrix} =: \boldsymbol{\delta}_n^n(\boldsymbol{\xi}^-) \tag{33}$$

where Eqs. (7), (16), and (24) are used to obtain the above equation. Finally, we integrate Eq. (17), respectively, until either $\xi_1 = \xi_1^+$ or $\xi_1 = \xi_1^-$, which implies either not being able to complete a step and returning to the initial configuration of this step, or a complete step is achieved. We denote the final state as $\xi_2^- = \Phi_{\alpha_n}(\boldsymbol{\xi}^+)$.

The entire slip recovery process is therefore represented by state transiting in the HZD space. Starting from the moment right before the slip impact, the initial zero dynamics state $\boldsymbol{\xi}^- \in \boldsymbol{S} \cap \boldsymbol{Z}_{\alpha_n}$ is mapped by $\boldsymbol{\delta}_n^s$, $\boldsymbol{\Psi}_s$, $\boldsymbol{\delta}_s^n$, $\boldsymbol{\Phi}_{\alpha_r}$, $\boldsymbol{\delta}_n^n$, and $\boldsymbol{\Phi}_{\alpha_n}$ successively. The returned value of ξ_2 after the slip recovery process is expressed as the composition of these mappings, namely

$$\xi_2 = \boldsymbol{\Phi}_{\alpha_n} \circ \boldsymbol{\delta}_n^n \circ \boldsymbol{\Phi}_{\alpha_r} \circ \boldsymbol{\delta}_s^n \circ \boldsymbol{\Psi}_s \circ \boldsymbol{\delta}_n^s(\xi_2^-) =: \rho_s(\xi_2^-) \tag{34}$$

For stable periodic normal walking gait, choosing Poincaré section as $\boldsymbol{\xi}^- \in \boldsymbol{S} \cap \boldsymbol{Z}_{\alpha_n}$, from Ref. [9], the Poincaré first return map has a stable fixed point ξ_2^-, namely

$$\xi_2^- = \Phi_{\alpha_n} \circ \delta_n^n(\xi_2^-) = \rho(\xi_2^-) \tag{35}$$

and

$$\frac{\partial \rho}{\partial \xi_2}(\xi_2^-) < 1 \tag{36}$$

These properties guarantee the existence of an invariant region $\boldsymbol{R} \subset \boldsymbol{S} \cap \boldsymbol{Z}_{\alpha_n}$ such that for a given $\xi_2^- \in \boldsymbol{R}$, any $\xi_2 \in \boldsymbol{R}$ satisfies

$$|\rho(\xi_2) - \xi_2^-| \leq |\xi_2 - \xi_2^-| \tag{37}$$

[3]We here use the subscript to virtual constraint $\boldsymbol{h}$ to indicate the gait profile α_r.

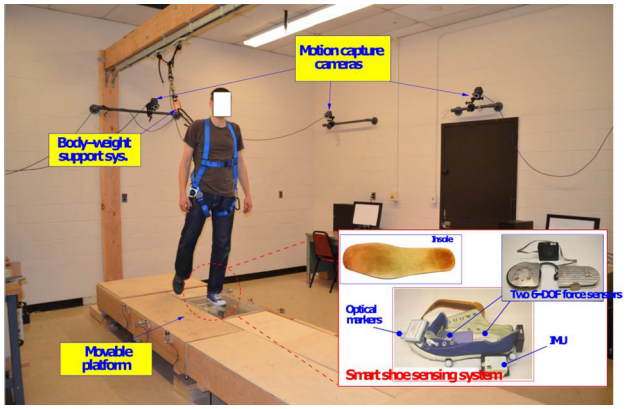

Fig. 3 The slip and fall experimental setup with various sensor suites

In the HZD space, the successful slip recovery to the normal gait is equivalent to $\xi_2 = \rho_s(\xi_2^-) \in \boldsymbol{R}$.

5 Experiments and Results

We conducted the indoor walking experiments on a wooden platform. Figure 3 shows the experimental setup of this study. The human subjects walked on the wooden platform in the laboratory. The human subject was first asked to walk on the platform to become familiar with the testing environment before the slip trial. A portion of the platform was painted with a soap film to create slip and recovery gaits when the subject stepped on the slippery surface. The segment with the reduced coefficient of friction was not noticeable to the subject such that the subject kept the normal gait before slip started.

The human walking gait was captured by the optical motion tracking system (8 Bonita cameras from Vicon Inc., Oxford Metrics, Oxford, UK) A small wireless inertial measurement unit model slimAHRS from Motion Sense Inc., Hangzhou, China) was also attached to each shoe to obtain the kinematic information of the foot and potentially for slip detection. Two 6DOF force/torque sensors (model SS-1 from INSENCO Co., Ltd, Hangzhou, China) were located inside the shoe to measure the 3D GRF and torques of the foot-floor contact; see Fig. 3. These 6DOF force sensors are thin (around 12–17 mm in thickness) and the human kept normal walking gait when wearing the shoes with embedded force sensors. The force and torque measurements were transmitted through wireless network to the host computer. The GRF sensors and the motion capture system were synchronized for data collection. The details of discussion about the experimental setup are reported in Ref. [21].

We first test and validate the foot rolling geometry using the normal walking motion data. Figure 4(*a*) shows the foot COP trajectory in the ankle frame. The data confirm the circular shape of the rolling model with radius $R = 0.22$ m with its center located at $(0.015, 0.096)$ m in the ankle frame. We use these estimated values in the bipedal model. Figure 4 shows the comparison results of the seven joint angles by the model prediction and the experiments of normal walking gait. We present these results over a normalized stance S due to the symmetry between the left and right legs. The stance is defined as the time duration from stance foot heel-touch to toe-off. The human subject walks at a speed of around 1.2 m/s and the double-stance consists of around 28% of the entire gait cycle. As shown in Fig. 4, the model predictions (solid lines) match the experiments (dash lines) closely for both the single-stance and double-stance phases. Figure 5 further shows the comparison results of the GRF (i.e., F_n and F_x) of the stance leg. Unlike the diverge results in the literature (e.g., Ref. [13]), the model prediction results follow the trend of the measurements from the force sensors. The discontinuity of the predicted GRF

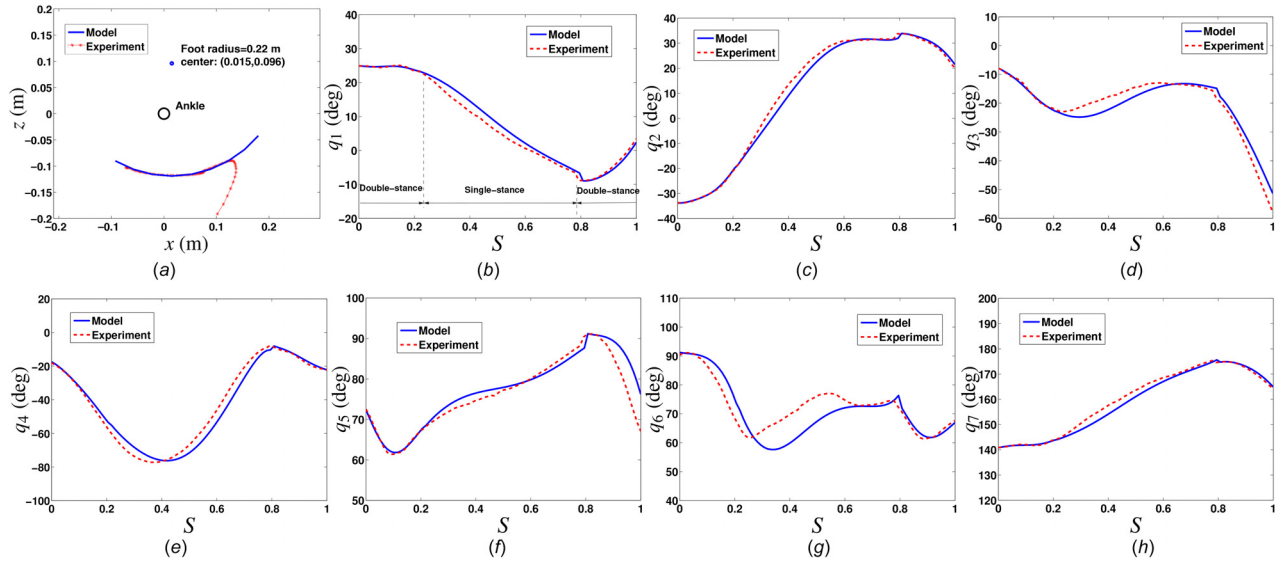

Fig. 4 (*a*) Experimental data to calculate the foot-floor contact rolling geometry. The red stars indicate the COP trajectory in the ankle frame and the blue curve is the fitting circular rolling shape. (*b*)–(*h*) Joint angle (q_1–q_7) comparison between the model prediction and the experiments during normal gait over one stance. The solid lines represent the model predictions and the dash lines show the experimental data.

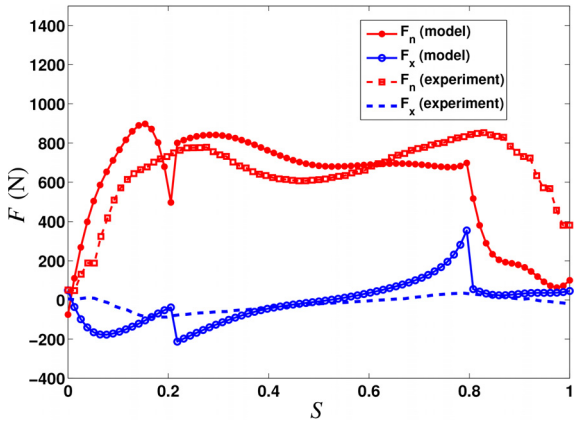

Fig. 5 The GRF (F_n and F_x) of the stance leg during the walking gait without slips

takes place at the phase switching moments due to the calculation errors of the joint angle accelerations from the single-stance and the double-stance models.

We next demonstrate the model prediction results for slip recovery gait experiment. Figure 6(*a*) shows a video snapshot of the slip recovery gait. The human subject starts the normal gait with a single-stance phase (i.e., $\mathcal{S}_1$ in Fig. 2) at $t = 0$ s. At $t = 0.32$ s, the (left) swing leg touches down on the slippery floor and then starts slipping. At this moment, the (right) foot is still in touch with the floor without slip and the human gait lies in double-stance slip phase ($\mathcal{S}_4$). Then at $t = 0.61$ s, the (right) swing foot leaves the ground (toe-off) and the (left) stance foot still slips. Therefore, the gait enters the single-stance slip phase ($\mathcal{S}_3$). The subject quickly notices and reacts to the slip occurrence. At $t = 0.96$ s, the (right) swing foot touches down, the (left) stance foot leaves the ground and the gait becomes a recovered single-stance phase without slipping ($\mathcal{S}_1$). Figures 6(*b*) and 6(*c*) show the human skeleton poses measured by the motion capture system and constructed by the model predicted joint angles, respectively.

Figure 7 shows the seven joint-angle comparison results of the measurements by the motion capture system and the model predictions considering double-support stance phase. The results clearly confirm that the model prediction follows the experiments closely during the entire gait recovery process. Figure 7(*h*) shows the slipping distance results and the model prediction follows the profiles from the experiments. Figures 8(*a*) and 8(*b*) show the normal and tangential GRF for both feet. The GRF comparison shows that except for the double-stance slip phase during $t = 0.32$–0.61 s, the normal and tangential GRF predictions match the measurements. During the double-stance slip period, the force prediction are however not accurate. Possible improvement of these double-stance force calculations could be achieved by increasing the order of the Bézier polynomials, adding additional term in the objective function (9) to follow the COM acceleration with respect to the gait α_d ($\mathrm{COM}(\alpha_d)$), or enhancing the GRF distribution between the legs by imposing additional force constraints. Figure 8(*c*) shows the RCOF, computed as $\mathrm{RCOF} = F_t/F_n$, of the stance-foot contact during the slip recovery process. Before slip starts (at around 0.32 s), the values of RCOF lie in a range of $|\mathrm{RCOF}| < 0.2$, which is far less than the available foot-floor friction coefficient (measured close to 1 of the dry rubber-wood contact [21]). At $t = 0.32$ s, the available COF is less than 0.05 due to the soap film on the surface. As shown in Fig. 8(*c*), the RCOF is nearly constant at around 0.05, which is lower than the available COF. Therefore, slip starts immediately when the foot touches down.

Next, we present a HZD prediction results for a multistep slip recovery. Figure 9 demonstrates a complete transition starting from normal walking stance (0–0.81 s), followed by a single-stance slip phase (0.81–1.28 s) and then single-stance recovery phase (1.28–2.40 s) and finally transitions back to a periodic normal walking gait. Figures 9(*a*)–9(*g*) show the joint angle comparison results of the model prediction and experiments, while Fig. 9(*h*) shows the slipping distance comparison. Note that the simulation results consider only a single-stance and impact mapping neglecting double-stance. The entire recovery follows the process given in Eq. (28). The HZD model prediction results match the experiments during the slip recovery and transition to the periodic walking gait process. The slight difference in phase timings of the HZD model prediction might be due to the inaccurate parameters values used in the simulation comparing with the experiments. The simulation of the single-stance recovery phase predicts a shorter duration as compared to the experiments. We suspect that in the experiment, the subject might apply a flat foot

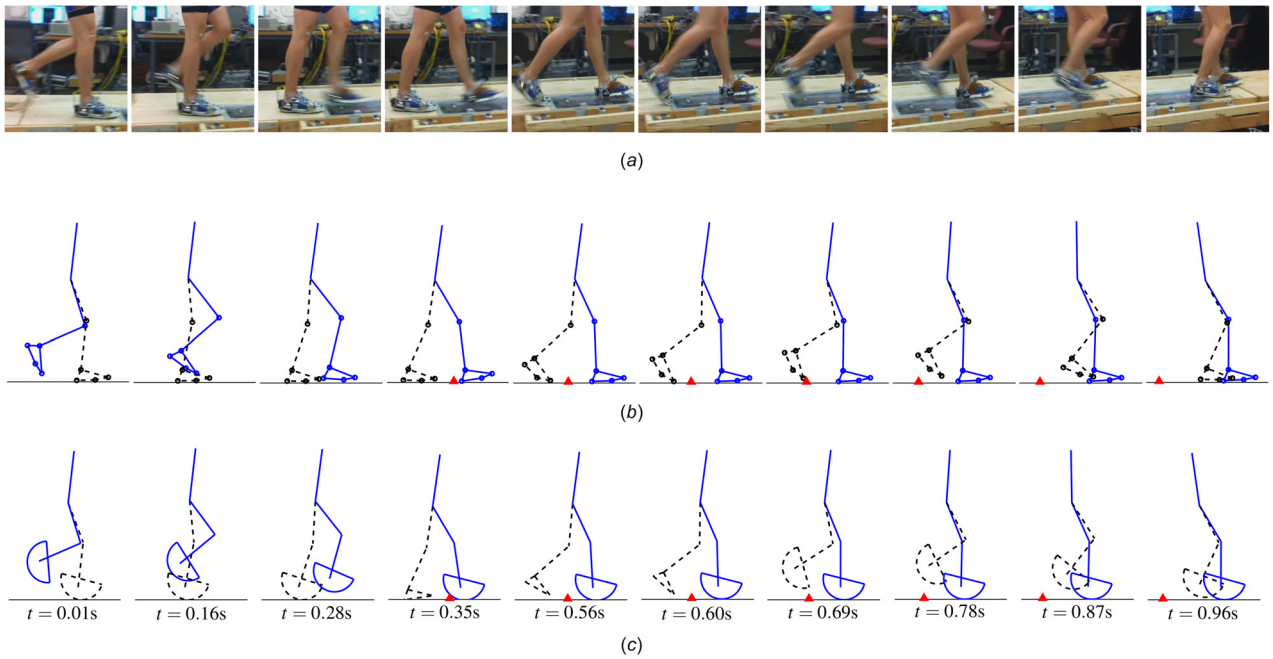

Fig. 6 A snapshot of the recovery human gait from slip. (*a*) Video snapshot. (*b*) Human 7-link skeleton from the optical motion capture system. The empty-circle dots indicate the reflective optical marker locations. (*c*) Skeleton prediction by the bipedal model. In (*b*) and (*c*), a red triangle is plotted to indicate the location where the left leg starts slipping. The right leg and trunk are represented by a solid blue line and the left leg by a black dash line.

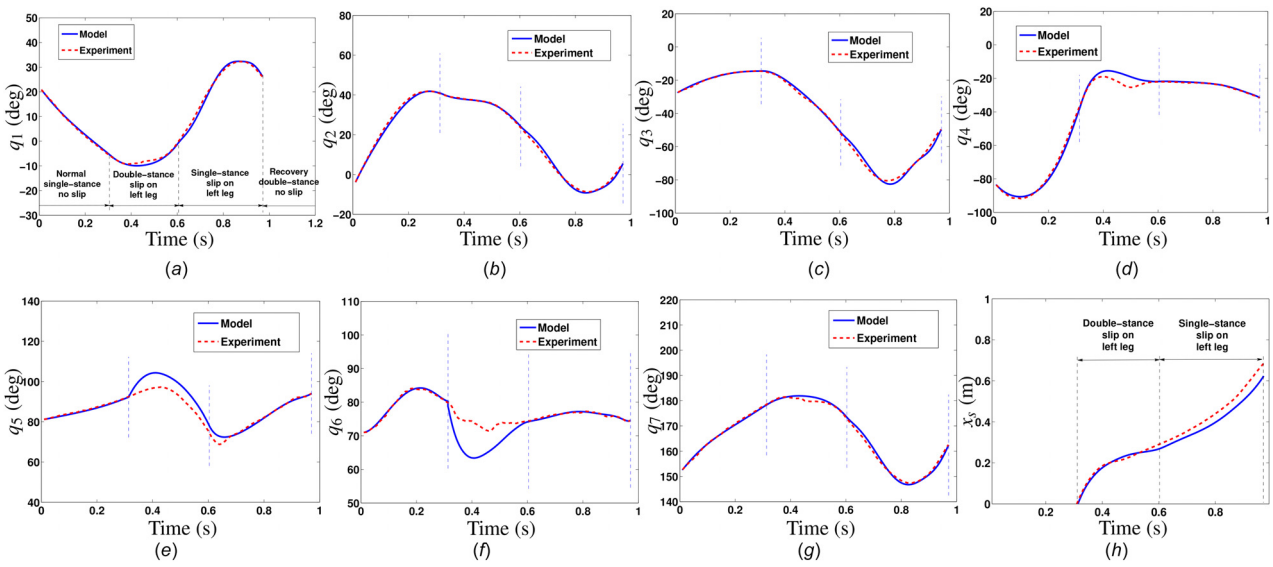

Fig. 7 ((*a*)–(*g*)) Joint angle (q_1–q_7) comparisons between the model prediction and the experiments during slip recovery gait. The solid lines represent the model predictions and the dash lines show the experimental data. (*h*) Slipping distance x_s of the (left) stance leg during the slip recovery experiment.

and it can be viewed as a fully actuated inverted pendulum with ankle torque control. This ankle torque control can reshape the time constant of the used underactuated inverted pendulum model. Our simulation does not consider this effect and instead adopts circular shaped feet during the slip recovery process.

Figure 10 shows the phase portraits of the zero dynamics for the recovery process. Figure 10(*a*) illustrates the 3D phase portrait in the $\xi_1/\dot{\xi}_{1s}$–$\xi_2/\dot{\xi}_{2s}$–x_s coordinates and Fig. 10(*b*) shows the phase portrait in the ξ_1–ξ_2 plane. Comparing with the normal walking gait, it is clear that the walking with foot slip generates much richer zero dynamics characteristics. The slip recovery process is on a high-dimensional manifold and consists of multiple portions of the phase portraits in 3D space as shown in Fig. 10(*a*). The HZD model predictions for the normal walking $\mathcal{S}_n$ (gait profile α_n, i.e., solid blue curves) and foot-slip gait $\mathcal{S}_s$ (impact $\mathcal{H}_n^s$ and gait profile α_s, i.e., solid red curve) match with the experiments, that is, solid blue and empty red circular markers, respectively. Moreover, as shown in Fig. 10(*b*), after the single-stance slip phase $\mathcal{S}_s$, the subject tried to recover from the slip by taking non-slip impact (blue dash-dot line) and then slip-to-normal recovery gait $\mathcal{S}_n(\alpha_r)$ (black dot curve for model prediction and square dots for experiments).

In Fig. 10(*b*), we also mark each individual mapping $\boldsymbol{\delta}_n^s$, $\boldsymbol{\Psi}_s$, $\boldsymbol{\delta}_s^n$, $\boldsymbol{\Phi}_{\alpha_r}$, $\boldsymbol{\delta}_n^n$, and $\boldsymbol{\Phi}_{\alpha_n}$, which together forms the composite

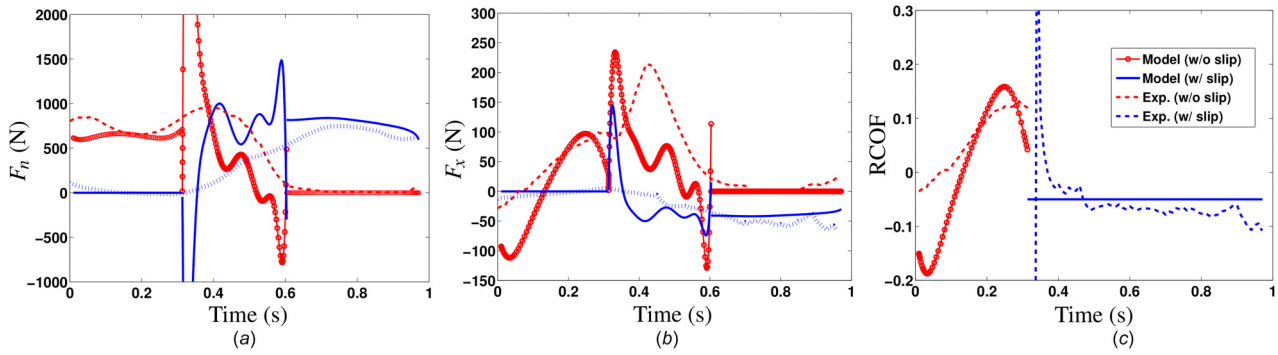

Fig. 8 Comparison results of the GRF and the RCOF during the slip recovery. (*a*) Normal GRF F_n, (*b*) tangential GRF F_x, and (*c*) RCOF of the stance leg foot. In (*a*) and (*b*), the model prediction forces for the left and right legs are plotted as the blue solid and red circle lines, respectively, and the experiments are plotted as the blue dotted and the red dash lines. In (*c*), the model predicted and experimental RCOF in nonslip phase is plotted by the red empty circle and the dash lines, respectively, and these in the slip phase by the blue solid and dash lines, respectively.

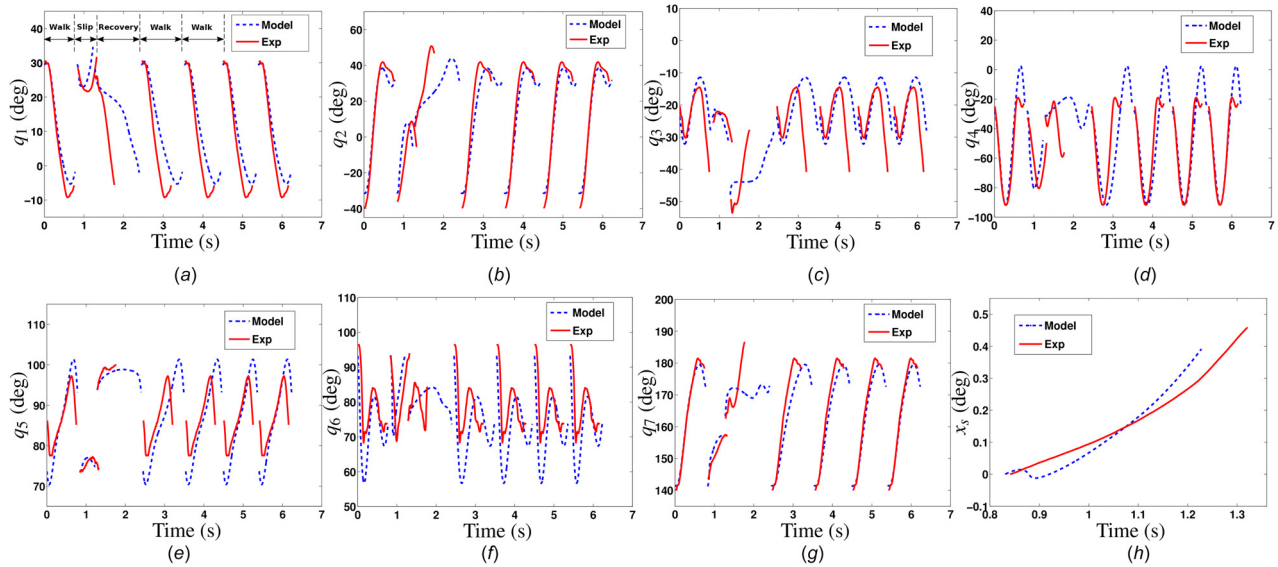

Fig. 9 ((*a*)–(*g*)) Joint angle (q_1–q_7) comparisons between the HZD model prediction and the experiments during the transition from a normal walking to slip recovery and multistep transition to a periodic walking gait. (*h*) Slipping distance x_s of the (left) stance leg during the slip recovery experiment.

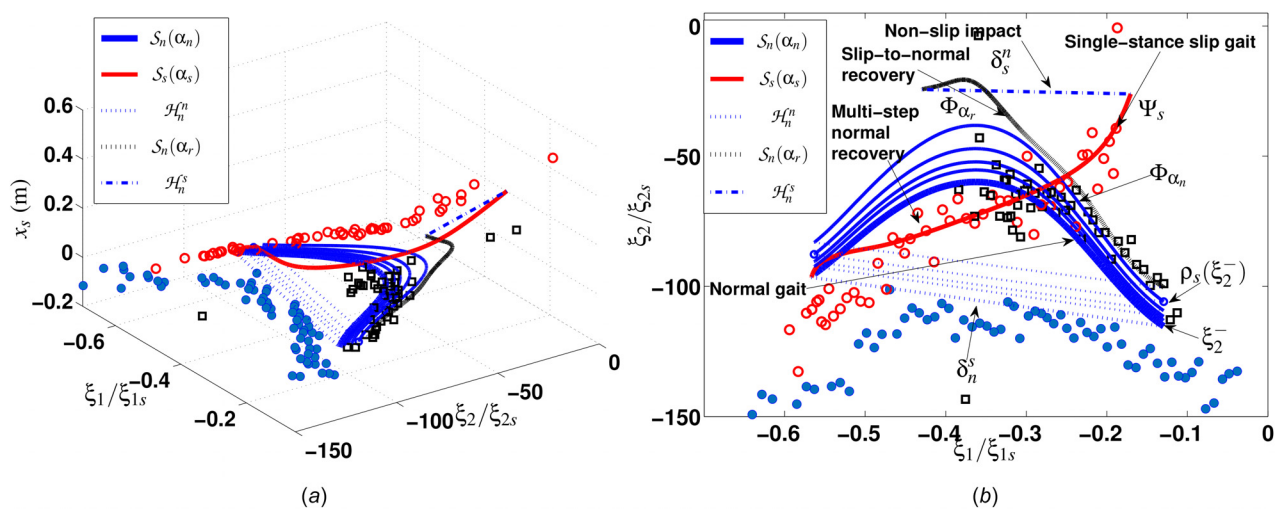

Fig. 10 (*a*) Three-dimensional phase portrait (ξ_1/ξ_{1s}–ξ_2/ξ_{2s}-x_s) during the slip recovery process. (*b*) 2D phase portrait in the ξ_1/ξ_{1s}–ξ_2/ξ_{2s} plane. In both plots, the empty circles and the empty squares are the experimental data during the phases $\mathcal{H}_n^s$ and $\mathcal{H}_s^r$, respectively. The solid circles are experimental data during normal walking phase $\mathcal{S}_n$ with gait profile α_n.

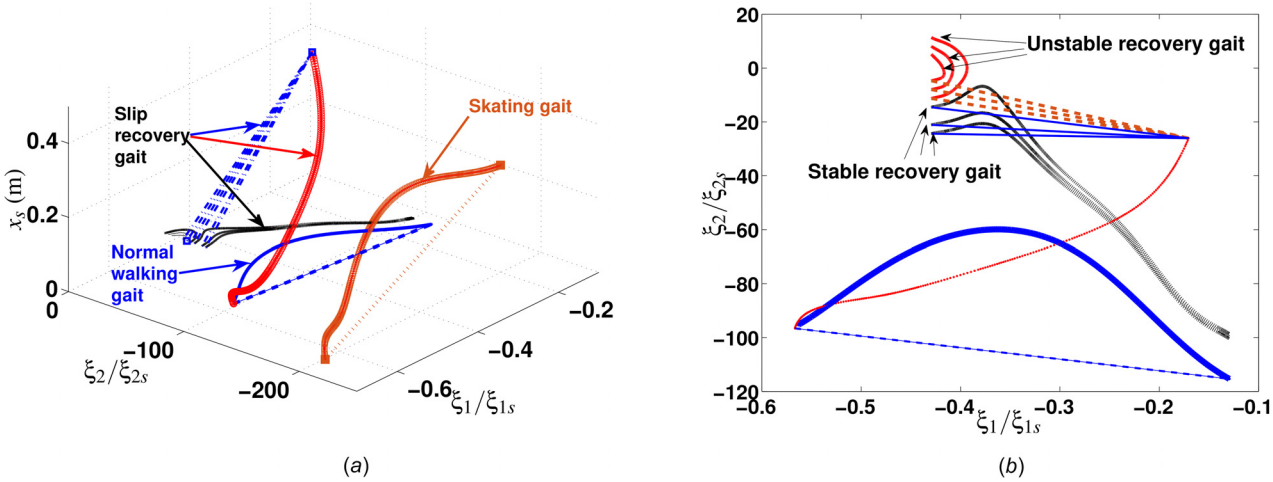

(*a*) (*b*)

Fig. 11 (*a*) Phase portraits of the normal walking gait, slip recovery gait, and skating gaits in 3D space and (*b*) phase portrait of the successful and unsuccessful slip recovery gaits in the $\xi_1/\xi_{1s}-\xi_2/\xi_{2s}$ plane

contracting return mapping ρ_s in Eq. (34) from pre-impact state ξ_2^- to recovery state $\rho_s(\xi_2^-)$. These mappings clearly show the slip recovery process and also the invariant region $\boldsymbol{R}$ defined by Eq. (37). We further analyze the HZD for various motions and gaits and show that the model can predict stable and unstable recovery. Figure 11(*a*) shows a collection of the phase portraits of the normal walking gait, slip recovery gait, and skating gaits in the ξ_{1s}–ξ_{2s}–x_s space. The steady skating gait is generated by considering both slipping and walking gaits as the skilled human motor locomotion. It is clear that the zero dynamics of the normal walking gait are located in the ξ_1–ξ_2 plane, while the skating gait is in the 3D space with motion in the x_s direction. The slip recovery gait consists of a series of transient motion that deviates from and then returns to the normal walking gaits. Figure 11(*b*) further illustrates the slip recovery gaits in which both successful, stable recovery (blue and black curves) and unsuccessful, unstable recovery (dash and solid red curves) gaits are plotted. Both sets of recovery gaits are obtained by enforcing the same virtual constraints. The only difference between these two trajectories is the value of $\boldsymbol{b}_n$ in Eq. (7) of the impact from slip gait to recover gait. The difference of $\boldsymbol{b}_n$ in Eq. (7) gives different initial ξ_2 values for the recovery gait, which indicates the falling angular moments. Once the value of ξ_2 passes through zero and becomes positive, the progression variable $\xi_1 = \theta$ is in a decreasing trend and this implies that the gait cannot be completely recovered. Figure 6(*c*) demonstrates the gait profiles for a successful slip recovery.

6 Discussion

One of the main goals of this study was the development of a bipedal model for analytical analysis of slip balance recovery. We recruited a single subject in our experiments and that is sufficient to serve the validation of the model development. The bipedal model and analysis can be applied to study walking and slip gait of any subject for whom the kinematic data are known. The model parameters (i.e., link lengths and masses) and joint angle trajectories are subject specific and need to be tuned for each individual. This paper does not provide generalization of slip balance recovery strategies across a wide population, since this would require analysis of multi-subject slip balance recoveries and is out of the scope of this paper.

During normal walking, the deviation between model and experimental results of the ankle angle (q_6) trajectory (see Fig. 4(*g*)) is primarily due to the approximation of using curved feet compared to the realistic human feet that have multi-DOFs. The circular feet can only roll on the ground and have a single point contact that coincides with the COP location. This is different compared to the human foot, which during single stance phase lays flat while COP progresses forward. These differences reflect also in the GRF profiles as shown in Fig. 5, where discrepancies between the model and experimental results exist primarily during double stance phase. At that instant, the toes of the swing (trailing) foot push-off the ground and generate additional forces, while the circular foot only rolls forward and does not have these capabilities. These differences originate from the discrepancies between the actual foot-floor rollover shape and circular foot approximation during the end of the stance as shown in Fig. 4(*a*). The differences between the model's rigid circular foot and the human's flexible foot complicate exact matching of the ankle angles during double stance slip phase. Slip occurrence during that phase further complicates exact matching. The use of circular foot was validated to be a reasonable approximation but however it is impossible to guarantee exact matching of all the joint angles throughout the whole stance, due to the reduced number of degrees-of-freedom compared to the human anatomical foot. The differences between foot orientation in the experiments and the model's circular foot in Fig. 6 are due to the reason that the model's circular foot is rolling on the ground and has a point contact, compared to the human foot that can lay flat on the ground while changing location of a COP within the foot support.

The limitation of this work is that the model considers only sagittal plane motion. While this captures the most important walking and slip characteristic, the inclusion of motion and foot placement in a lateral plane can further explain overall slip balance recovery and provides a complete analysis of the human response during slip perturbations.

7 Conclusions and Future Work

This paper presented a robotic bipedal dynamic model and the extended HZD for human walking gait with foot slip. We relaxed the nonslip assumption used in the existing bipedal robotic models and explicitly modeled the foot slipping on the ground. A general hybrid bipedal model and the gait controllers were developed for human walking with foot slip. The presented HZD was an extension of the existing dynamics for normal walking locomotion. We explicitly derived and presented the HZD for human walking with foot slip that contains two additional zero dynamics states. It is interesting to show that the HZD under foot slip presented rich human motor skills, including the normal walking, slip recovery gaits, and highly skilled skating motion. Stability condition for slip recovery gait was discussed, and the HZD-based recovery simulation and experiments were also successfully demonstrated.

We plan to extend the HZD model to further analyze the motion stability and dependency on the model parameters and motion

variables. We are also working on how to design virtual gait constraints and slip recovery strategies that can lead to stable HZD under foot slip. Integration of the modeling and analysis of the stable HZD and the gait control under foot slip with robotic assistive devices is another future research direction.

Acknowledgment

The work was partially supported by NSF under awards CMMI-1334389 and CMMI-1762556. The authors thank the members of the Robotics, Automation, and Mechatronics (RAM) Lab at Rutgers for their help.

Funding Data

- NSF (Award No. CMMI-1334389 and CMMI-1762556; Funder ID: 10.13039/501100008982).

References

[1] Stevens, J. A., Corso, P. S., Finkelstein, E. A., and Miller, T. R., 2006, "The Costs of Fatal and Non-Fatal Falls Among Older Adults," Inj. Prev., **12**(5), pp. 290–295.
[2] Burns, E. R., Stevens, J. A., and Lee, R., 2016, "The Direct Costs of Fatal and Non-Fatal Falls Among Older Adults–United States," J. Saf. Res., **58**, pp. 99–103.
[3] U.S. Department of Labor, 2016, "Bureau of Labor Statistics," U.S. Department of Labor, Washington, DC.
[4] Redfern, M. S., Cham, R., Gielo-Perczak, K., Grönqvist, R., Hirvonen, M., Lanshammar, H., Marpet, M., Pai, C. Y., and Powers, C., 2001, "Biomechanics of Slips," Ergonomics, **44**(13), pp. 1138–1166.
[5] Yang, F., and Pai, Y.-C., 2010, "Reactive Control and Its Operation Limits in Responding to a Novel Slip in Gait," Ann. Biomed. Eng., **38**(10), pp. 3246–3256.
[6] Patton, J., Pai, Y.-C., and Lee, W. A., 1999, "Evaluation of a Model That Determines the Stability Limits of Dynamic Balance," Gait Posture, **9**(1), pp. 38–49.
[7] Mahboobin, A., Cham, R., and Piazza, S. J., 2010, "The Impact of a Systematic Reduction in Shoe-Floor Friction on Heel Contact Walking Kinematics—A Gait Simulation Approach," J. Biomech., **43**(8), pp. 1532–1539.
[8] Dingwell, J. B., and Kang, H. G., 2006, "Differences Between Local and Orbital Dynamic Stability During Human Walking," ASME J. Biomech. Eng., **129**(4), pp. 586–593.
[9] Westervelt, E. R., Grizzle, J. W., Chevallereau, C., Choi, J. H., and Morris, B., 2007, *Feedback Control of Dynamic Bipedal Robot Locomotion*, CRC Press, Boca Raton, FL.
[10] Grizzle, J. W., Chevallereau, C., Sinnet, R. W., and Ames, A. D., 2014, "Models, Feedback Control, and Open Problems of 3D Bipedal Robotic Walking," Automatica, **50**(8), pp. 1955–1988.
[11] Srinivasan, S., Raptis, I. A., and Westervelt, E. R., 2008, "Low-Dimensional Sagittal Plane Model of Normal Human Walking," ASME J. Biomech. Eng., **130**(5), p. 051017.
[12] Martin, A. E., and Schmiedeler, J. P., 2014, "Predicting Human Walking Gaits With a Simple Planar Model," J. Biomech., **47**(6), pp. 1416–1421.
[13] Srinivasan, S., 2007, "Low-Dimensional Modeling and Analysis of Human Gait With Application to the Gait of Transtibial Prosthesis Users," Ph.D. thesis, Ohio State University, Columbus, OH.
[14] Hansen, A. H., Childress, D. S., and Knox, E. H., 2004, "Roll-Over Shapes of Human Locomotor Systems: Effects of Walking Speed," Clin. Biomech., **19**(4), pp. 407–414.
[15] Westervelt, E. R., Grizzle, J. W., and Koditschek, D. E., 2003, "Hybrid Zero Dynamics of Planar Biped Walkers," IEEE Trans. Autom. Control, **48**(1), pp. 42–56.
[16] Chen, K., Trkov, M., Yi, J., Zhang, Y., Liu, T., and Song, D., 2015, "A Robotic Bipedal Model for Human Walking With Slips," IEEE International Conference on Robotics and Automation (ICRA), Seattle, WA, May 26–30, pp. 6301–6306.
[17] Chen, K., Trkov, M., and Yi, J., 2017, "Hybrid Zero Dynamics of Human Biped Walking With Foot Slip," American Control Conference (ACC), Seattle, WA, May 24–26, pp. 2124–2129.
[18] Grönqvist, R., Chang, W.-R., Courtney, T. K., Leamon, T. B., Redfern, M. S., and Strandberg, L., 2001, "Measurement of Slipperiness: Fundamental Concept and Definitions," Ergonomics, **44**(13), pp. 1102–1117.
[19] Kong, K., and Tomizuka, M., 2009, "A Gait Monitoring System Based on Air Pressure Sensors Embedded in a Shoe," IEEE/ASME Trans. Mechatronics, **14**(3), pp. 358–370.
[20] Liu, T., Inoue, Y., Shibata, K., and Shiojima, K., 2012, "A Mobile Force Plate and Three-Dimensional Motion Analysis System for Three-Dimensional Gait Assessment," IEEE Sensors J., **12**(5), pp. 1461–1467.
[21] Trkov, M., Yi, J., Liu, T., and Li, K., 2018, "Shoe–Floor Interactions in Human Walking With Slips: Modeling and Experiments," ASME J. Biomech. Eng., **140**(3), p. 031005.
[22] Zhang, Y., Chen, K., Yi, J., and Liu, L., 2014, "Pose Estimation in Physical Human-Machine Interactions With Application to Bicycle Riding," IEEE/RSJ International Conference on Intelligent Robots and Systems (IROS), Chicago, IL, Sept. 14–18, pp. 3333–3338.
[23] Chevallereau, C., Djoudi, D., and Grizzle, J. W., 2008, "Stable Bipedal Walking With Foot Rotation Through Direct Regulation of the Zero Moment Point," IEEE Trans. Rob., **24**(2), pp. 390–401.
[24] Braun, D. J., and Goldfarb, M., 2009, "A Control Approach for Actuated Dynamic Walking in Biped Robots," IEEE Trans. Rob., **25**(6), pp. 1292–1303.
[25] Zhao, H.-H., Ma, W.-L., Zeagler, M. B., and Ames, A. D., 2014, "Human-Inspired Multi-Contact Locomotion With AMBER2," ACM/IEEE International Conference on Cyber-Physical Systems (ICCPS), Berlin, Germany, Apr. 14–17, pp. 199–210.
[26] Spong, M. W., Hutchinson, S., and Vidyasagar, M., 2006, *Robot Modeling and Control*, Vol. 3, Wiley, New York.